SANDIA REPORT

SAND2018-11244
Unlimited Release
Printed Sept. 2018

Data Analysis for the Born Qualified LDRD Project

Laura P. Swiler, Bart van Bloemen Waanders, Bradley Jared, Josh Koepke, David Saiz, Shaun Whetten, Brad Boyce, Jonathan Madison, Thomas Ivanoff, Olivia Underwood, Adam Cook, Harlan Brown-Shaklee, Dan Kammler, Kyle Johnson, Kurtis Ford, Joseph Bishop, Allen Roach

Prepared by
Sandia National Laboratories
Albuquerque, New Mexico 87185 and Livermore, California 94550

Sandia National Laboratories is a multimission laboratory managed and operated by National Technology and Engineering Solutions of Sandia, LLC, a wholly owned subsidiary of Honeywell International, Inc., for the U.S. Department of Energy's National Nuclear Security Administration under contract DE-NA0003525.

Issued by Sandia National Laboratories, operated for the United States Department of Energy by National Technology and Engineering Solutions of Sandia, LLC.

Available to DOE and DOE contractors from
U.S. Department of Energy
Office of Scientific and Technical Information
P.O. Box 62
Oak Ridge, TN 37831

Telephone: (865) 576-8401
Facsimile: (865) 576-5728
E-Mail: reports@osti.gov
Online ordering: http://www.osti.gov/scitech

Available to the public from
U.S. Department of Commerce
National Technical Information Service
5301 Shawnee Rd
Alexandria, VA 22312

Telephone: (800) 553-6847
Facsimile: (703) 605-6900
E-Mail: orders@ntis.gov
Online order: https://classic.ntis.gov/help/order-methods/

SAND2018-11244
Printed Sept. 2018
Unlimited Release

Data Analysis for the Born Qualified LDRD Project

Laura Swiler, Bart van Bloemen Waanders
Optimization and Uncertainty Analysis 1441
Sandia National Laboratories
P. O. Box 5800
Albuquerque, New Mexico 87185-MS1318

Bradley Jared, Josh Koepke, David Saiz, Shaun Whetten
Coatings and Additive Manufacturing1832
Sandia National Laboratories
P. O. Box 5800
Albuquerque, New Mexico 87185-MS0958

Jonathan Madison, Thomas Ivanoff, Olivia Underwood
Materials Mechanics and Tribology Dept. 1851
Sandia National Laboratories
P. O. Box 5800
Albuquerque, New Mexico 87185-MS0889

Brad Boyce
Nanostructure Physics Dept. 1881
Sandia National Laboratories
P. O. Box 5800
Albuquerque, New Mexico 87185-MS0889

Adam Cook
Advanced Materials Laboratory Dept. 1815
Sandia National Laboratories
P. O. Box 5800
Albuquerque, New Mexico 87185-MS1349

Harlan Brown-Shaklee
Electronic, Optical, and Nano Dept. 1816
Sandia National Laboratories
P. O. Box 5800
Albuquerque, New Mexico 87185-MS1411

Dan Kammler
Applied Science & Technology Maturation 2585
Sandia National Laboratories
P. O. Box 5800
Albuquerque, New Mexico 87185-MS0878

Kyle Johnson, Kurtis Ford, Joseph Bishop
Component Science and Mechanics Dept.1556
Sandia National Laboratories
P. O. Box 5800
Albuquerque, New Mexico 87185-MS0346

R. Allen Roach
Advanced and Exploratory Systems Dept. 2241
Sandia National Laboratories
P. O. Box 5800
Albuquerque, New Mexico 87185-MS0156

Abstract

This report summarizes the data analysis activities that were performed under the Born Qualified Grand Challenge Project from 2016-2018. It is meant to document the characterization of additively manufactured parts and processes for this project as well as demonstrate and identify further analyses and data science that could be done relating material processes to microstructure to properties to performance.

ACKNOWLEDGMENTS

We gratefully acknowledge the support of the Laboratory Directed Research and Development (LDRD) program and the support of Greg Frye-Mason, the manager of the LDRD program.

TABLE OF CONTENTS

1. INTRODUCTION

1.1. Paradigm Shift in Qualification with AM parts

Additive Manufacturing (AM) is a flexible, agile production pathway ideal for low volume, high value, high consequence, complex parts [1,2]. The rapid turnaround for AM parts can improve long cycle times of the traditional design-build-test-refine cycles we currently use. However, there are multiple technical challenges that must be addressed to achieve a paradigm shift in qualification using the promise of AM. Today, AM processes suffer from challenges with variability in part quality due to build-to-build inconsistencies, inadequate dimensional tolerances, surface roughness, grain size, and defects [3, 4]. These challenges result in costly and time consuming post-build processes (e.g. Hot Isostatic Pressing, machining) to inspect or remediate internal defects (porosity, cracks), alter material properties (strength, ductility), or introduce surface modifications (finish, tolerance). Minimizing these added post-build processes is strongly desirable for financial and qualification needs. Having the ability to predict properties, structure, and performance of AM builds allows for the use of optimization for part performance and the ability to eliminate or reduce post-build processing.

Inherent to the paradigm shift needed to change qualification is the integration of computational and physical models that comprise of a range of material options and incorporate multiple length and time scales. These models are critical to understand the Process-Structure-Property-Performance (P-S-P-P) connectivity that is difficult or impossible to deduce experimentally. Utilizing integrated models to produce a validated, predictive capability integrated with real-time and ex-situ diagnostics is the foundation of a new approach. The technical challenges to achieve this new design and qualification paradigm can be divided into five key areas.

1. Novel real-time AM diagnostic tools to quantify and monitor critical AM process variables for materials control and optimization.

2. Innovative and rapid experimental techniques to calibrate and validate models as well as correlate materials performance to in-process diagnostic measurements.

3. Computational models to relate process conditions to microstructure and ultimately to bulk measurable properties.

4. Approaches to characterize, model, and control variability in AM processes.

5. Intelligent data collection from various and diverse sources to develop science-based heuristics.

As highlighted in Figure 1.1, using the capabilities of AM integrated with a validated, predictive capability and real-time and ex-situ diagnostic tools facilitates creation of a framework to translate AM Process results to material properties by relating microstructure to bulk measurable properties to ultimately predict component performance.

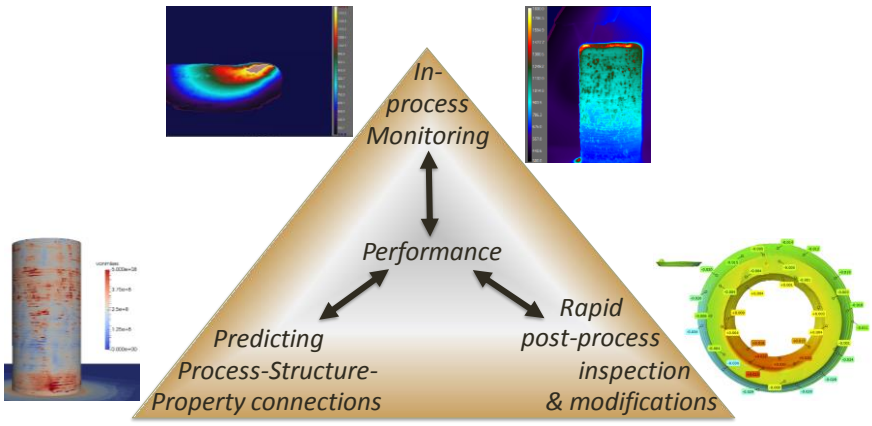

Figure 1.1: General P-S-P-P approach used in a new Qualification Paradigm

The Born Qualified Grand Challenge project has developed advances in all five areas above. In this report, we focus primarily on items 4 and 5, specifically methods to analyze and characterize variability, perform uncertainty quantification both with respect to experimental data and computational models, and develop data science methods to address to large volume of data being generated, both from the AM builds and the AM characterization.

The Born Qualified project has developed a new framework for qualification, as shown in Figure 1.2, that relies extensively on optimization and uncertainty quantification as foundations. Data analysis and uncertainty quantification happens in every one of the light colored boxes in Figure 1.2 (e.g. properties alinstante, process and in-situ diagnostics, and models) as well as in the robust control and validation tasks.

Data science [5,6], and uncertainty quantification problem [7-10] are critical to address the qualification challenge. Overall the goal is to use optimization as the interface between numerical simulation, experiments, data, and uncertainties; map numerical capabilities to real experiments; and use data science in each part of the P-S-P-P map. To provide maximum information and create robust solutions in the face of uncertainties, the development of a research strategy for intelligent data collection and analysis of diverse sources (experiments, diagnostics, models) requires generating, filtering, selecting, and sampling data. To transform practices, we need to be able to characterize uncertainties at all stages: at the raw material stage, during the AM process, in the resulting microstructure of the material created in the AM process, and ultimately, in the product created from that material. These uncertainties are characterized by enormous sets of experimental data, materials models across all length scales, and AM process models. Efficient techniques are needed to propagate parameter uncertainties through models, including sampling, stochastic expansions, interval analysis, and reliability methods. The ability to fully couple numerical multi-scale simulators with efficient analysis tools is necessary so that models can be calibrated, used in an optimal design process, and can eventually guide the

manufacturing process.[11] Techniques must also be developed and implemented to calibrate model parameters with incorporated experimental uncertainty.

Materials characterization, "Properties Alinstante", experimental design, integration of AM modeling with micro-meso-macro scale modeling, optimal control, and risk-averse design optimization all play important roles in managing and characterizing uncertainties in the overall product development and qualification as shown in Figure 1.2. This new qualification framework utilizes a multi-scale approach that is rapid and flexible where performance is predicted probabilistically and the manufacturing process is tightly controlled. The computational and statistical methodologies exist to achieve end-to-end uncertainty quantification, but the integration with large data sets, many scales of material models, and preliminary AM models makes this task very challenging.

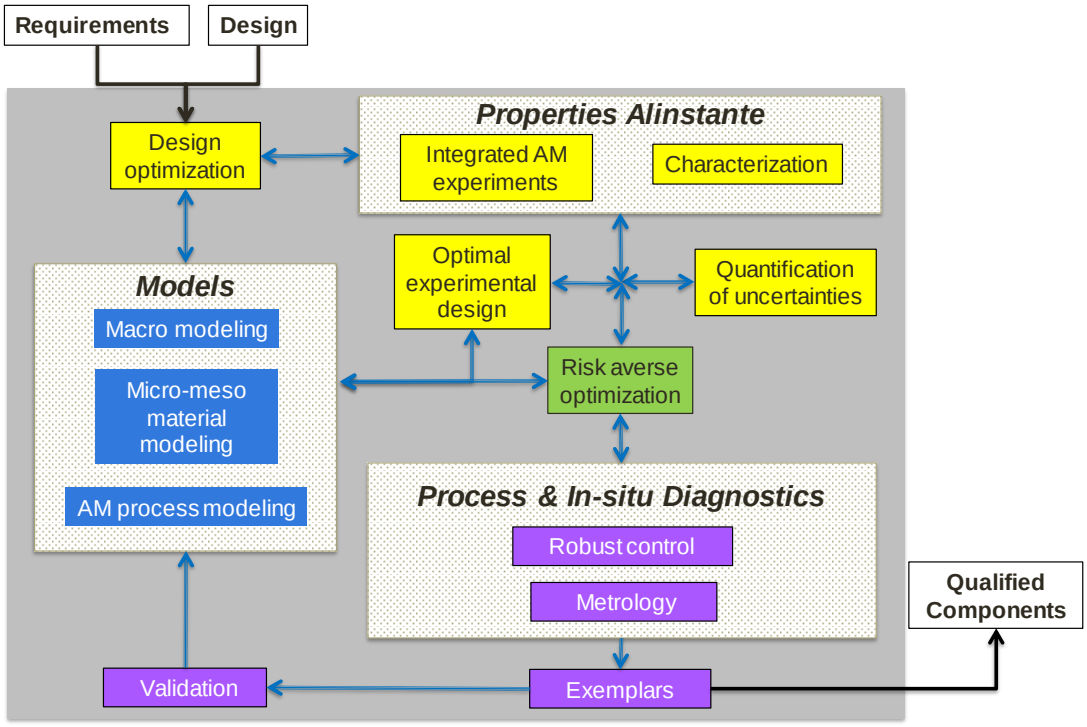

Figure 1.2: Framework for new AM-driven Qualification Paradigm

1.2. Data Science and Uncertainty Quantification

There are several underlying data science capabilities that will be used to analyze both the experimental and model data to create the process-structure-property linkages. These include the following:

- Statistical analysis capabilities
  - Analysis of measurement information from processes
  - Analysis of distributional information from parts made additively.

- Microstructure analysis (e.g. from CT data, modeling, microscope data)
    - 2-point correlation [12,13]
    - Spectral Density Function [14]
- Design of experiments
    - Basic testing of machine performance, replicability, machine settings
    - Factors important to a particular part or design
- Surrogate models
    - Models relating processes to part properties.
    - May be a simple functional relationship (linear or nonlinear regression model, spline or neural network model, Gaussian process) or a computational model
    - Could be a machine learning algorithm operating on a "feature set" of information. For example, one might use a classfier to predict if an AM layer is acceptable or not, based on in-situ temperature/ pressure/etc. measurements.
- Data management and storage
    - Methods to archive large amounts of disparate data (from scalar quantities to static images to movies to 3-D time-dependent results from computational simulations).
    - Dedicated server being set up to interface to AM machines for storage of data
    - Dimension reduction algorithms
    - Feature extraction algorithms
    - Data compression algorithms

The various data science approaches used in Born Qualified will be highlighted in the chapters below when discussing particular parts and/or processes. In this document, we report progress with respect to the three AM technology areas of focus: Powder Bed (metal), LENS (metal), and Direct Write (ceramic). The data available and analysis done for each AM process is documented in Chapters 2, 3, and 4, with some summary recommendations made in Chapter 5.

2. POWDER BED

In laser powder bed fusion (PB), a laser scans across successive layers of metal powder to fuse material and generate a desired part geometry.[15] Such layerwise processing offers access to volume elements, i.e. voxels, throughout every part and therefore unprecedented opportunities for material control. Localized material control, however, also introduces the opportunity to produce defects at any point during the build process. Distinct from traditional subtractive processes, component geometry and material are formed concurrently and preclude an a priori knowledge of material performance based solely on feedstock properties. Further, characterizing, controlling and predicting material performance is commonly difficult for powder bed processes since it involves complex melting and solidification interactions, and is implemented on equipment with limited capabilities for process control and/or defect tracking.

In this chapter, we describe three sets of data we had relative to laser powder bed fusion.

2.1. Gen 1 Tensile specimens

Prior to the start of the Born Qualified project, Sandia had two external vendors produce arrays of 17-4PH stainless steel tensile bar specimens to demonstrate high-throughput tensile testing and analysis. This dataset (called "Generation 1" or Gen1) was used in part to develop data analysis and uncertainty quantification capabilities until Sandia-produced tensile specimens were available for Born Qualified. In Gen1, there were two commercial vendors who each produced an additively manufactured set of 120 tensile bars in 20 rows by six columns as shown in Figure 2.1. The basic geometry of the tensile bar is shown in Figure 2.2. Sandia produced a special test fixture to pull these tensile bar specimens as shown in Figure 2.3.

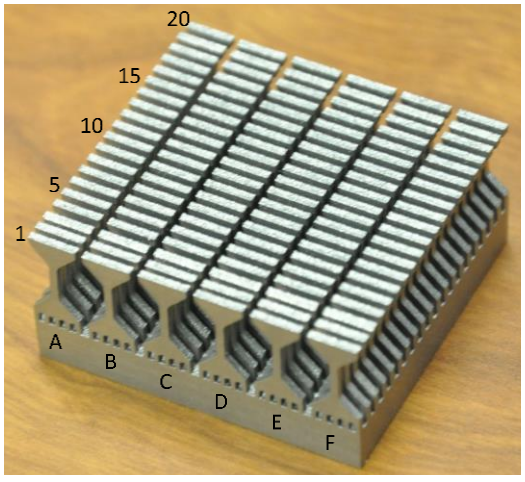

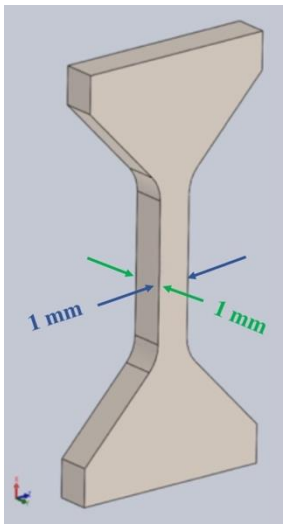

Figure 2.1. Additively manufactured tensile bars built in a 120 sample build array of 6 columns and 20 rows (left). Figure 2.2. The individual tensile bar geometry (right).

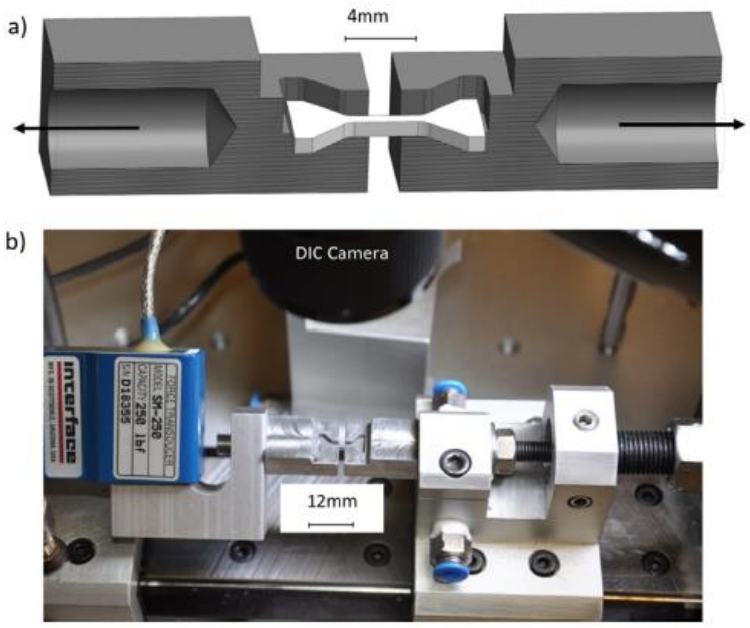

Figure 2.3. Model of AM tensile specimen in grips (a), mechanical test set-up (b).

The PB tensile bars (called dogbones) exhibited slightly lower strength and markedly lower ductility compared to wrought product. Moreover, the properties were much less repeatable in the AM materials as analyzed in the context of a Weibull distribution, and the properties did not consistently meet minimum allowable requirements for the alloy as established by AMS. The main properties analyzed were ultimate tensile strength, yield strength, and ductility.

The results of the first study with the two arrays of 120 tensile bars from the two vendors were published in the paper "High-throughput stochastic tensile performance of additively manufactured stainless steel" [4]. Subsequently, Sandia contracted with one of the vendors to produce 9 arrays which were nominally produced under the same process settings. The variability within and across the 9 sets of builds was discussed in the paper "High-Throughput Stochastic Tensile Performance of Additively Manufactured Stainless Steel" [16].

The initial work on the Gen1 dogbones is documented in a final LDRD report on defect characterization [18]. Particular aspects that we focused on under Born Qualified were differences obtained with various estimation methods for three-parameter Weibull distributions and correlation analysis of the material properties. We also examined spatial variation of the properties across the build plate and the relationship of porosity information obtained from μCT scans of the tensile bars to their material properties [17]. In the sections below, we reference the published papers, but also provide some descriptions and examples of the data analysis methods used since these were also used in later analyses including Gen2.

2.1.1. *Three-parameter Weibull*

Weibull distributions were fit to ultimate tensile strength, yield strength, and ductility for the dogbones. Various statistical packages use different optimizers to optimize the parameters of a Weibull distribution that ``best fits'' the data. Even if they all use maximum likelihood estimation, we observed that the shape and scale parameter for the Weibull could vary depending on what was assumed about a threshold parameter (a value below which the distribution cannot take: a two parameter Weibull corresponds to a threshold value of zero). The statistical package JMP assumes that the threshold is the smallest observed value in the data set. Minitab is more flexible, and allows the user to choose or estimate a lower threshold. We also coded up a maximum likelihood routine in Matlab to check the nature of the likelihood function and ensure the statistical tools were giving reasonable results.

Differences in cumulative distribution functions for various choices of threshold values can make a big difference in tail probabilities. Based on examination of contour plots of likelihood function as a function of the three governing parameters, we found that the likelihood tends to have a well-defined optimum. Optimization of Weibull parameters generally should not be a problem but does depend on assumptions about threshold value. Different threshold values can result in Weibull distributions that are fairly similar but which can have big differences in tail probabilities, as shown in Figure 2.4. For example, the left side of this figure shows the differences in the cumulative distribution function values for various choices of threshold values. Although these three Weibull distributions look similar, they have a difference of around 36MPa for the estimate of the 0.001 quantile (from 926 to 962MPa) and a difference of 16MPa for the 0.01 quantile. If this is significant for a particular application (and we often care about the worst one percent, for example), then care should be taken to choose a lower threshold carefully when inferring tail probabilities.

	V2 Peak UTS Three Parameter Weibull		
	JMP	Minitab	User Threshold
Shape	5.94	63.05	7.52
Scale	103.3	1034	133.2
Threshold	929.9	0	900
P(X ≤ x)			
0.001	962.19	926.71	953.16
0.01	977.52	961.25	972.25
0.05	992.55	986.42	989.74
0.1	1000.62	997.75	998.75
0.25	1013.65	1013.77	1012.86
0.5	1027.02	1028.01	1026.86
0.75	1039.04	1039.37	1039.11
0.9	1048.77	1047.77	1048.82
0.95	1054.16	1052.15	1054.12
0.99	1063.49	1059.35	1063.19
0.999	1072.92	1066.19	1072.23

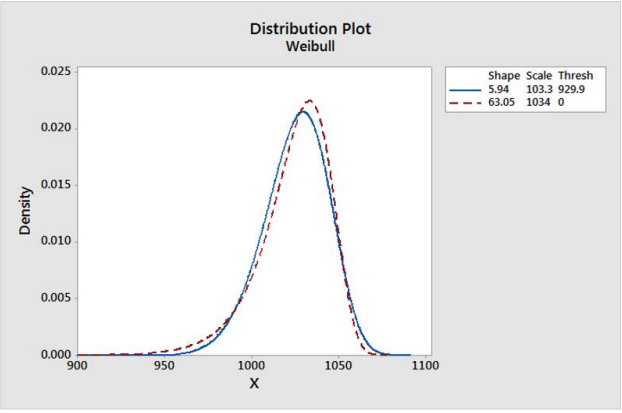

Figure 2.4. Weibull distribution differences for various choices of threshold parameter value (left) and differences in density function for the JMP and Minitab results (right).

2.1.2. *Correlation analysis*

Because we did not have process parameters with respect to the Gen1 dogbone data, we first examined correlation of the material properties (such as density, initial

unloading modulus, ultimate tensile strength, yield strength, and ductility). We initially found lower correlations than we expected between key parameters such as density and yield strength. As a reminder: a correlation coefficient varies between -1 and 1 and measures the strength and direction of a linear relationship between two variables. If the correlation is positive, that indicates that the second variable increases when the first variable increases. If the correlation is negative, that indicates that the second variable decreases when the first variable increases. If the correlation is 1.0 or -1.0, if you were to plot the data points from variables x1 and x2, they would lie along a line.

Correlations are generally considered very significant if they are greater than 0.5 in absolute value, and of moderate significance if they are between 0.25 and 0.5. Table 2.1 shows that there are some correlations across the material properties of the dogbones. Note that this data was taken with most of the 6*20 dogbones, but there were a few that were missing or were bad (specifically, row 20 and F15-F19), so the total number was 109. The results in Table 2.1 show that the initial modulus is highly correlated to several other material properties such as yield strength (correlation of 0.76) and elongation (UNFelg). Ductility and elongation are highly correlated (0.82) but the unexpected finding was that density was not highly correlated to other material properties.

	Density	*Mass*	*Z-score, ave*	*Modulus, initial*	*Modulus, unloading*	*Strength, yield*	*Strength, ultimate*	*UNFelg*	*Ductility*
Density	1.00								
Mass	0.27	1.00							
Z-score, ave	-0.13	-0.53	1.00						
Modulus, initial	0.00	0.26	-0.30	1.00					
Modulus, unloading	0.03	-0.03	0.19	0.21	1.00				
Strength, yield	-0.04	0.25	-0.35	0.76	-0.24	1.00			
Strength, ultimate	0.02	0.09	0.16	0.27	0.29	0.13	1.00		
UNFelg	0.12	-0.03	0.18	-0.58	-0.11	-0.52	0.10	1.00	
Ductility	0.17	0.24	-0.06	-0.34	-0.08	-0.33	0.18	0.82	1.00

Table 2.1. Initial correlation analysis of the Gen1 dogbones: all data used.

2.1.3. Spatial correlation across build plate

We examined the spatial pattern of the properties across the build plate. Two examples are shown in Figure 2.5, where the columns A-F are denoted across the bottom of the plate, and rows 1-19 along the side. The lower half of the build plate, rows 1-8, have noticeably higher yield strength and initial modulus than the upper half of the plate. It also appears that there is a feature or low spot for yield strength and initial modulus around C12-C18. We are not sure if this was due to a change in the process or some artifact from the manufacturing process since these were externally made and the vendor did not provide more details. Note the dark blue in the upper right corner is spurious: it is the missing F15-20 data.

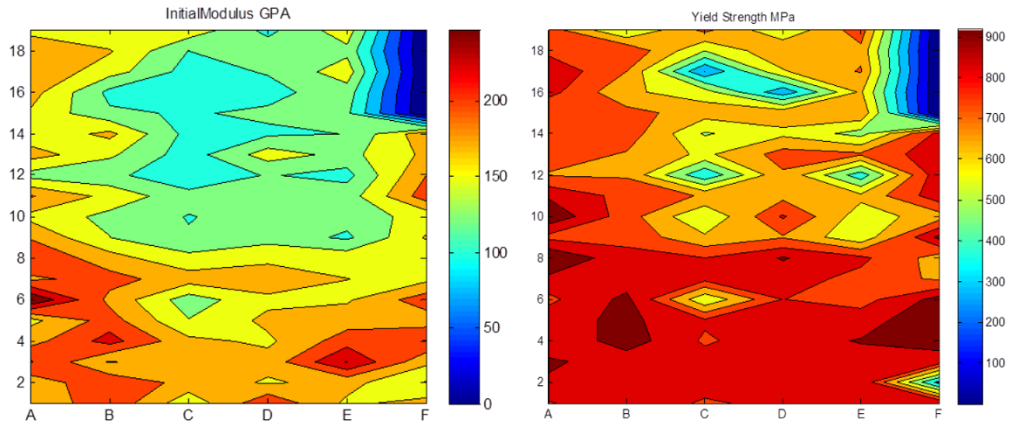

Figure 2.5: Contour plots of material properties across the build plate.

Since we have 15 scalar attributes describing the material properties for each dogbone, we utilized a data mining approach to see if anything further could be gleaned from the data. The 15 scalar attributes include density, mass, top face dimensions, initial and unloading modulus, yield and tensile strength, and ductility.

We performed k-means clustering, which is a statistical algorithm that partitions *n* data points (15-D data points in our case) into *k* different classes or clusters. The clusters are defined by their mean. Each observation or data point belongs to the cluster with the closest mean. This results in a partitioning of the data space into Voronoi cells.

K-means clustering worked effectively on this data set, partitioning it into 4 clusters. The clusters did have a strong spatial pattern as shown in Figure 2.6 (b), where the green cluster #3 is predominantly dogbones on the upper half of the build plate. We also show the clusters with respect to some of the inputs in Figure 2.6(a): they are clearly separable with respect to inputs such as yield strength and initial modulus, but not as separable with respect to others.

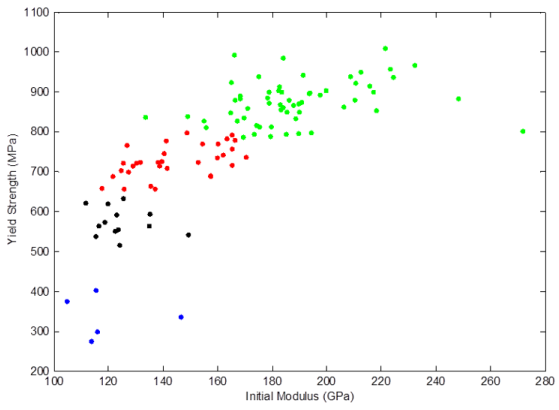

	A	B	C	D	E	F
1	3	3	3	3	3	3
2	3	3	3	3	3	2
3	3	3	3	3	3	3
4	3	3	3	3	3	3
5	3	3	3	3	3	3
6	3	3	4	3	3	3
7	3	3	3	3	3	1
8	3	3	3	3	3	1
9	3	1	1	1	4	3
10	3	1	4	3	4	1
11	3	1	1	1	1	3
12	1	1	2	1	2	3
13	3	1	4	1	1	3
14	1	3	4	4	4	3
15	1	1	1	1	1	
16	3	1	4	2	1	
17	3	1	2	4	1	
18	3	3	4	1	1	
19	1	4	1	4	1	

Figure 2.6. The four clusters identified over 15 material properties are projected onto two of the material properties (a) showing a delineation of the clusters. The four clusters were mapped onto the build plate (b), showing some correlation of clustering with respect to build location.

2.1.4. *Correlation of porosity information to material properties*

Micro-computed tomography was used to characterize the material volume of each dogbone in the 17-4PH correlation study. µCT provides detailed characterization of internal void structures which prompted extensive data analyses to identify inter-build correlations and trends with tensile properties.

Reference [17] captures details of the segmentation, 3D reconstruction and quantitative characterization of the 17-4PH µCT correlation study used for the tensile dogbones. Here we briefly describe the porosity metrics explored and the stepwise regression analysis used to identify the porosity metrics most informative in predicting the yield strength.

Note that the analysis of µCT data is very labor intensive and expensive. Each dogbone specimen generated about 600 TIFF images which had to be correctly cropped to the gage section and segmented. The segmentation process involves converting a gray-scale image to binary white and black pixels representing the presence or absence of material. Scripts then were written to generate the defect structure metrics, including total volume of defects, pore volume fraction, spatial location of all pores, total number of defects, defects per length, total distribution of defect volumes, total distribution of equivalent spherical diameters, total distribution of cross-sectional areas normal to the tensile axis and total distribution of nearest neighbor distances.

Scatterplots and linear regression lines for yield strength with respect to the defect metrics are shown in Figure 2.7.

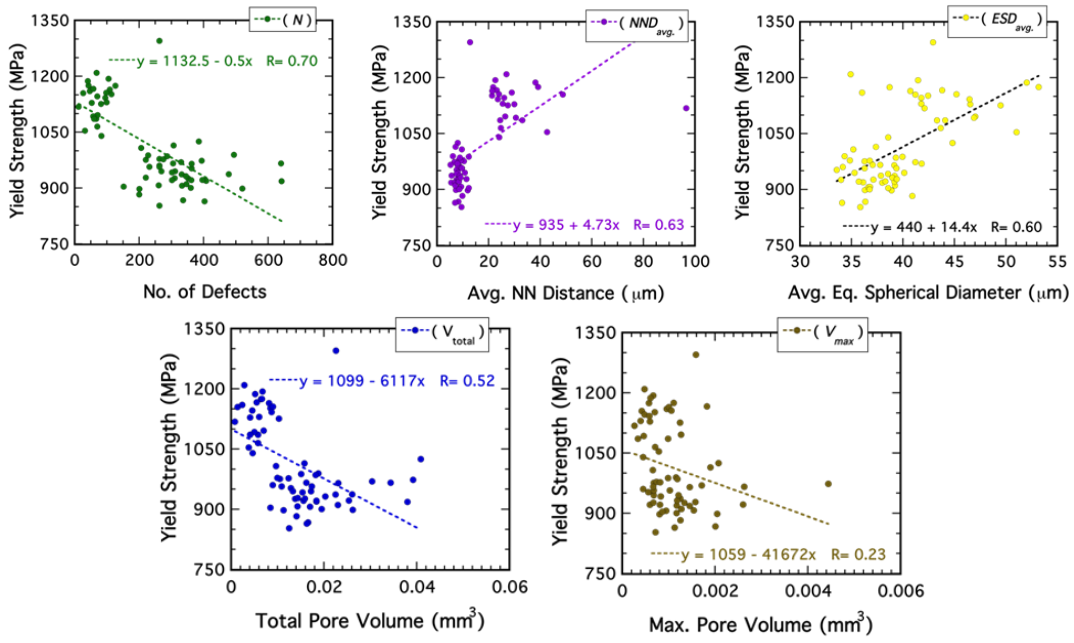

Figure 2.7. Scatterplots of Defect metrics (along x-axes) and yield strength (along y-axes) for 17-4 stainless steel Gen1 dogbone tests.

We then correlated the defect metrics to the material response properties. The results are shown in Table 2.2. It should also be mentioned that post-build bead-blasting was found to have significant non-uniform effects of external facing surfaces compared to their internal ones. As such, exterior facing samples were omitted from the following correlations. In Table 2.2, the correlation coefficient (R) and the coefficient of determination (R^2) are shown for each listed metric with respect to yield stress. No single correlation coefficient was found to exceed 70% and no single coefficient of determination value was observed to exceed 50%. The coefficient of determination refers to the amount of variance in the response that can be attributed to a particular variable. In this data, only half of the variation observed in yield strength can be related to the number of voids or defects. Thus, the strongest trend observed in the entire data set (yield strength verses total number of defects) exhibited a coefficient of determination of only 0.5.

Measure	**R**	**R^2**
Number of Defects	- 0.71	0.50
Average Nearest Neighbor Distance (mm)	0.63	0.40
Average Equivalent Spherical Diameter (mm)	0.60	0.36
Max Cross-sectional Area Reduction (mm^2)	-0.58	0.38
Total Pore Volume	-0.52	0.27
Average Defect Volume (mm^3)	0.50	0.25
Maximum Pore Size (mm^3)	-0.26	0.07

Table 2.2. Correlation coefficient (R) and the coefficient of determination (R^2) values for defect metrics on yield stress.

We used stepwise regression, which builds up a series of regression models involving one or more independent variables. Stepwise regression identifies the best (e.g. maximum R^2) model if you can only use one independent predictor variable, then the best if you can use two predictors, then three, etc. In this way, we examined the possibility of greater predictivity of yield stress based upon the combination of multiple individual measures, which is a multivariate regression. All seven measures shown in Table 2.2 were evaluated using a combinatorial approach which successively included a greater quantity of predictor variables measures. The results of this combinatorial multivariate regression on the coefficient of determination is shown in Table 2.3 where an "X" in the table indicates that predictor's measures inclusion in a linear regression attempt and the "no of metrics" column indicates the total number of measures utilized.

No. of Metrics	R^2	No. of Defects (N)	Avg. Defect Volume ($V_{avg.}$)	Avg. Equivalent Spherical Diameter ($ESD_{avg.}$)	Total Pore Volume (V_{tot})	Maximum Pore Volume (V_{max})	Average Nearest Neighbor Distance ($NND_{avg.}$)	Maximum Cross-Sectional Area Reduction (CSA_{redux})
1*	0.50	X						
1	0.40						X	
2*	0.55	X		X				
2	0.54	X	X					
3	0.58	X	X					X
3	0.58	X		X				X
4*	0.59	X	X				X	X
4	0.59	X			X		X	X
5	0.60	X	X		X		X	X
5	0.60	X		X	X		X	X
6	0.60	X	X	X	X		X	X
6	0.60	X		X	X	X	X	X
7	0.60	X	X	X	X	X	X	X

Table 2.3. Stepwise regression indicating the optimal defect metrics to predict yield stress.

Performing multi-variate regression with seven porosity metrics only raised R^2 to 0.6. This indicates that additional defect metrics in the regression do not help that much. The limited correlation observed in the µCT datasets reveals that the mechanical strength of the 17-4PH dogbones is influenced by more than internal porosity. Internal microstructure variations and exterior surface defects impact part strength and may account for much of the variation not captured by the µCT porosity correlations.

2.2. Gen 2 Tensile Specimens

"Generation 2" involved a large set of tensile specimens produced on the ProX200 machine at Sandia. The Gen2 specimens were 316L stainless steel, in contrast to Gen1 which were 17-4 stainless steel. The material response characterization of the Gen2 tensile dogbones involved the use of high throughput tensile test equipment that was designed by Brad Boyce here at Sandia. The test unit is shown in Figure 2.8 below. This test unit can hold an array of tensile test specimens, such as a cartridge containing 25 dogbone bars.

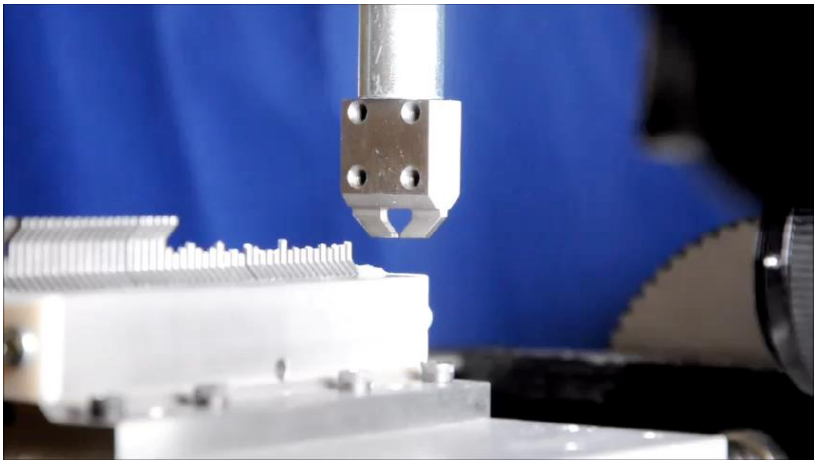

Figure 2.8. High throughput tensile tester used for Gen2 Dogbones.

In Gen2, there were a few build plates that were produced. The two main build plates had 10 arrays of 25 dogbones each. On one plate, laser power was varied across 10 different levels, with all of the other process parameters of the build held constant. On the second plate, scan velocity was varied across ten different levels. Thus, we had 10 settings for laser power and 10 settings for scan velocity.

An example of the build plate which had the variation of laser power is shown in Figure 2.9. Laser power was varied from 28% of the maximum power level to 58% of the maximum power level. Note that the 52, 55, and 58% levels failed: the parts were not well-formed as shown in Figure 2.9. Scan velocity varied from 1190 mm/s to 1750 mm/s on a separate build plate, and all levels of scan velocity succeeded in producing viable tensile specimens.

Each of the 10 settings of laser powder or scan velocity involved printing an array of 25 dogbones. For most of these results, each array had 20 of the 25 dogbones tested for material properties. The material properties characterized included: 0.5% yield strength from published modulus (MPa), 0.5% yield from unloading modulus, the unloading modulus (MPa), ultimate tensile strength (UTS), the work hardening rate, UNFelg (% elongation), ductility (%), and cross-sectional area of the tensile specimen (mm^2). We did build some plates that also varied the scan pattern and spacing between lines but these plates were not fully characterized. For the analysis below, we focus on laser power and scan velocity.

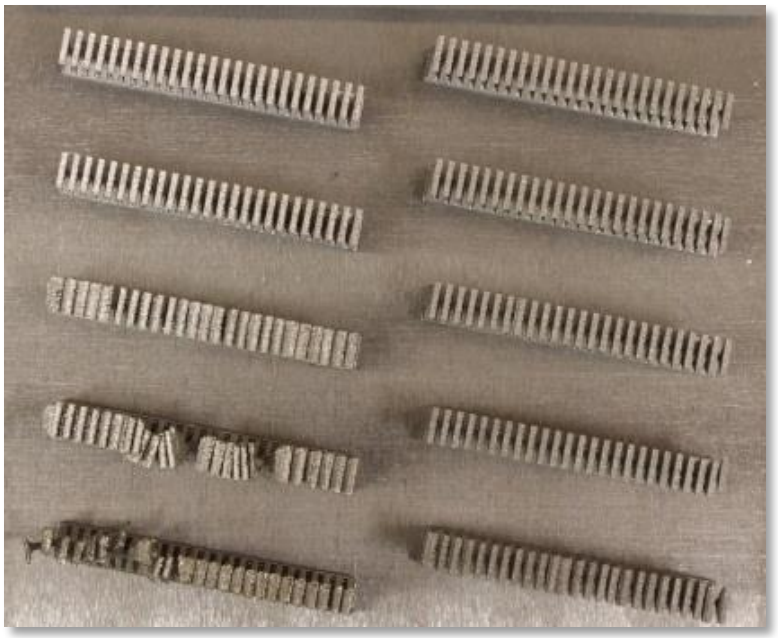

316L SS samples w/ varying laser power

Figure 2.9: Build Plate from ProX 200 with variations of laser power, with arrays at lower left having highest power levels (52, 55, and 58% of maximum power of 300W, or 156W, 165W, and 174W respectively) and failing.

Table 2.4 shows the correlation between material properties of the dogbone specimens. The same color scheme is used as in Table 2.1, where an absolute value of correlation between 0.5 and 1.0 is colored yellow (a high correlation) and an absolute value between 0.25 and 0.5 is colored orange (a medium correlation). The number of yellow and orange cells in this table indicates that there are very high correlations between the material property responses. Additionally, the two rows highlighted with the black box show the correlations of the process parameters (scan velocity and laser power) with respect to the material properties. Some of these correlations are very high.

	.5% yield (MPa) from pub. mod.	*.5% yield from unloading mod.*	*Unloading Mod. (MPa)*	*UTS*	*work hardening rate*	*UNFelg (%)*	*Ductility (%)*	*area (mm^2)*	*Velocity (mm/s)*	*Power (W)*	*Radiant energy density (J/mm^3)*	*Density (g/cm^3)*
.5% yield (MPa)	1.00											
.5% yield from unloading mod.	0.99	1.00										
Unloading Mod. (MPa)	0.82	0.80	1.00									
UTS	0.79	0.83	0.87	1.00								
work hardening rate	0.51	0.56	0.60	0.85	1.00							
UNFelg (%)	0.20	0.24	0.27	0.58	0.89	1.00						
Ductility (%)	0.01	0.06	0.14	0.45	0.79	0.92	1.00					
area (mm^2)	-0.84	-0.83	-0.67	-0.54	-0.14	0.19	0.33	1.00				
Velocity (mm/s)	0.70	0.67	0.41	0.30	0.10	-0.12	-0.32	-0.85	1.00			
Power (W)	0.19	0.21	0.20	0.48	0.78	0.83	0.79	0.11	0.00	1.00		
Radiant energy density (J/mm^3)	-0.50	-0.46	-0.27	-0.01	0.36	0.59	0.72	0.79	-0.79	0.60	1.00	
Density (g/cm^3)	0.25	0.29	0.39	0.65	0.89	0.86	0.79	0.19	-0.18	0.76	0.58	1.00

Table 2.3. Correlations between material properties and process parameters for Gen2 dogbones.

To summarize, laser power is strongly positively correlated with the work hardening rate, UNFelg, and ductility. Scan velocity is most strongly negatively correlated with area of the dogbone. As the velocity increases, the area decreases. Power and density are strongly correlated, but power is not particularly correlated with the yield strength numbers.

In addition to correlations, we plotted some of the material properties with respect to the process settings. These are shown in Figures 2.10 and 2.11, with the data points in blue and a best fit quadratic trend line in red. Note that Figure 2.10 shows only the results from the build plate where power was varied, and 2.11 shows only the results from the build plate where scan velocity was varied.

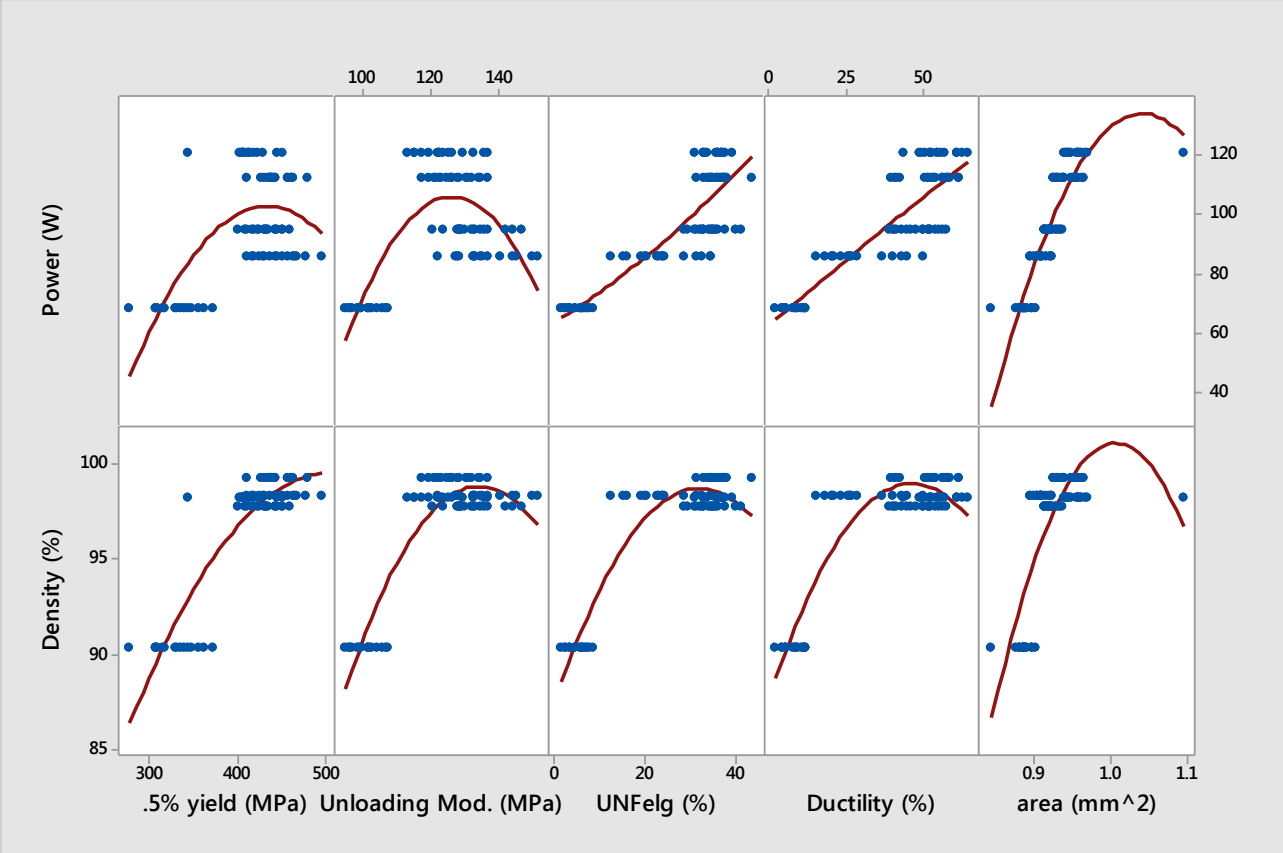

Figure 2.10. Scatterplots and fitted quadratic trends of power and density with respect to material properties. This data is from the build plate varying power only.

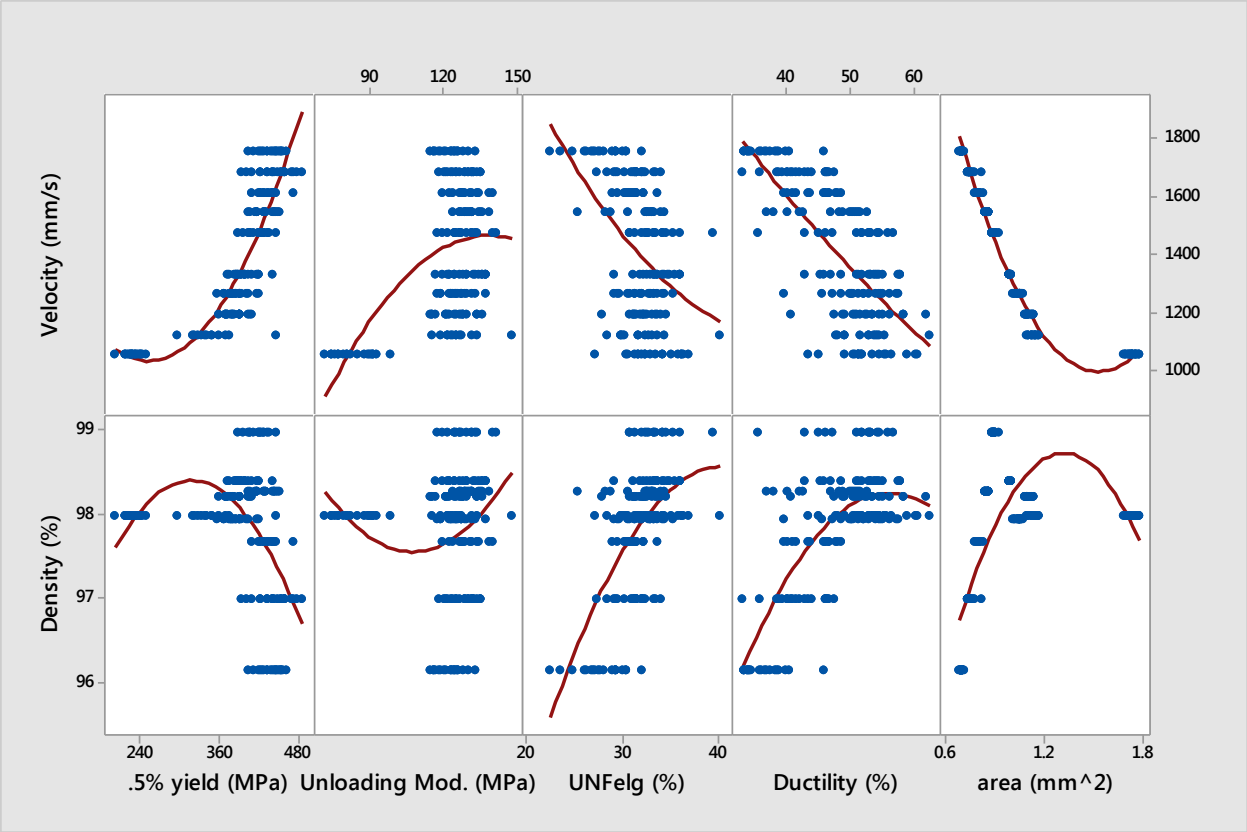

Figure 2.11. Scatterplots and fitted quadratic trends of velocity and density with respect to material properties. This data is from the build plate varying scan velocity only.

2.2.1. *Radiant Energy Density*

In the AM community, a common metric to plot results from a variety of additive processes is radiant energy density which accounts for factors such as the layer thickness, the beam diameter, the scan velocity, and the laser power. The formula is given below:

$$Radiant\ Energy\ Density\ \frac{J}{mm^3} = \frac{LaserPower\ (Watts)}{ScanVelocity\ \left(\frac{mm}{s}\right) * LayerThickness\ (mm) * BeamDiameter(mm) * cross\ feed\ factor}$$

Where $cross\ feed\ factor = 1 + \%overlap * \frac{cross\ feed(mm)}{beam\ diameter(mm)}$

As an example, consider a build with the following values values: Laser Power (103 W), Scan Velocity (1400mm/s), Layer thickness (30 µm, 0.03 mm), Beam Diameter (100 µm, 0.1 mm), cross feed % overlap 0.5%, cross feed 50 µm. For this case, radiant energy density = 19.62 J/mm^3.

The results from the Gen2 tensile tests is shown in Figures 2.12 and 2.13, where quadratic fits were made to the data for the specimens where power was varied (in orange) or scan velocity was varied (in grey). These graphs show that because radiant energy density combines several of the process parameters, it is a useful predictor for some of the material response characteristics such as yield and tensile strength. These R^2 values are generally higher than can be achieved with predicting yield strength as a function of laser power or scan velocity alone.

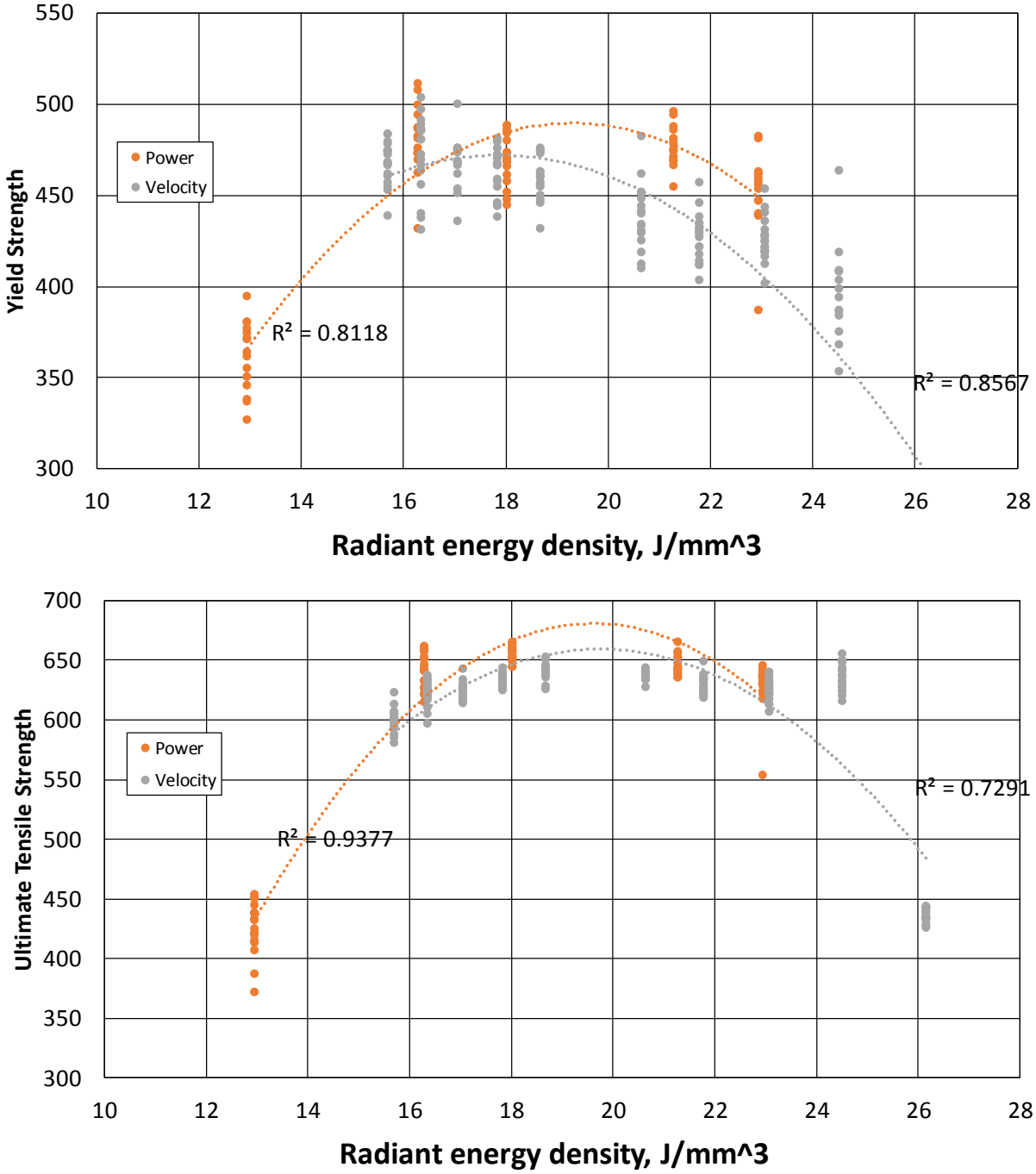

Figure 2.12. Gen2 strength results plotted against radiant energy density, with quadratic fits.

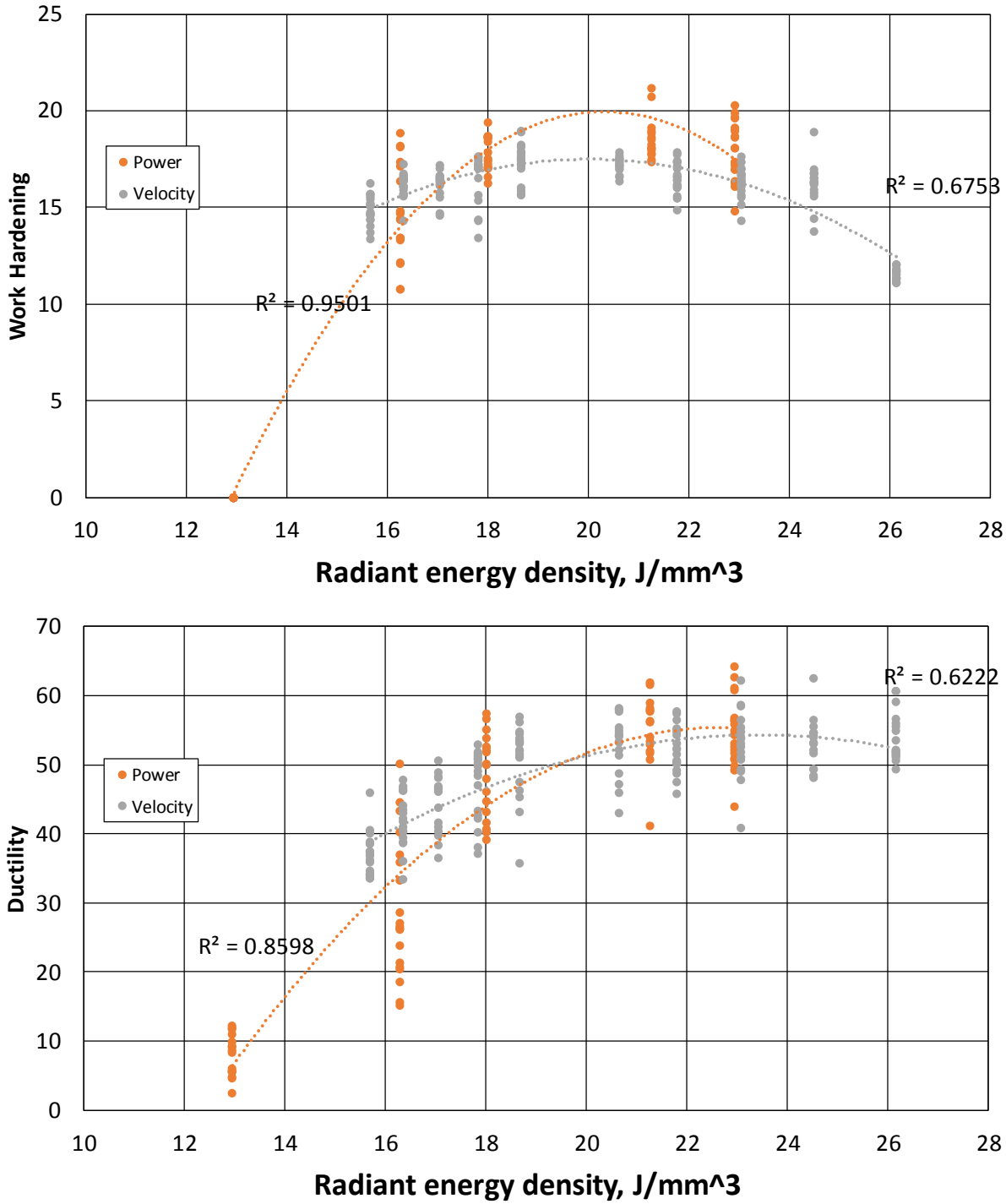

Figure 2.13. Gen2 hardening and ductility results plotted against radiant energy density, with quadratic fits.

Figures 2.12 and 2.13 indicate that there is an optimal process regime (a "process plateau") where the various material properties tend to be fairly optimal and not too sensitive to the radiant energy density. This process regime is around 16-20 J/mm3, depending on the material response metric being optimized. These conclusions are

specific to the ProX200 machine and this particular set of studies, but it indicates the possibility of a robust process regime.

2.2.2. Void analysis of Gen2

In contrast to the Gen1 dogbones, where micro-computed tomography was used to characterize the material volume of each dogbone in the full array of over 100 dogbones, we only have 7 Gen2 dogbones that went through a μCT scan. These dogbones included the following:

Power A (112W), Power I (low value of 68W), Velocity A (1470 mm/s), Velocity J (low value of 1070 mm/s), and three hatch patterns: mesh, normal, and hex. All of the hatch patterns were done at the nominal values of power (103W and 1400mm/sec). The hex pattern is the default pattern used on the ProX200 machine.

Thomas Ivanoff performed the image processing, segmentation, and data analysis shown below. Note that the image processing and segmentation was significant: some of the specimens were bent or warped, which creates issues with locating voids because the material edges significantly shift in the image frame. The workflow for the analysis of the micro-computed tomography is shown in Figure 2.14.

After the images are processed and segmented into regions which have material (denoted in white in Figure 2.14) vs. voids (in black), the image processing software can calculate the number of voids, the volume of the voids, the average nearest neighbor distance between voids, etc. These void metrics were then plotted against the material properties. This is shown in Figures 2.15-2.18.

Figure 2.15 shows a comparison of the void metrics across the specimens. This figure shows that the tensile bar produced at the low Power I is an anomaly that has extreme porosity, with a much larger number of voids and void volume (and corresponding smaller average nearest neighbor distance) than the other specimens. The other specimens show good consistency across the void metrics. For Fig 2.15, the minimum volume and equivalent spherical radius both describe the size of the smallest void that is detectable. The minimum volume (151 um^3) and the minimum equivalent spherical radius (3.3 um) describing that volume are equivalent.

A better comparison of the variability across the specimens can be seen in Figure 2.16 when we exclude Power I. This figure shows the variability in the metrics is significant. For example, the range of the number of voids is over 300 voids (from approximately 400 to 700) with a mean of 550 voids. Similarly, the range on the average void volume is 7E-7mm^3, from 6E-7mm^3 to 13E-7mm^3, with a mean slightly over 9 mm^3. With these few specimens, one must be cautious about overinterpreting trends. There are a few things to note, however, from Figure 2.16. The mesh build pattern showed a higher number of voids and larger void volume than the normal or hex pattern. The mesh tensile bar was bent, which could have contributed to this. The other interesting aspect to note is that the slower velocity, Velocity J, appeared to have very good results with respect to the void metrics. More CT scans and a study of larger scope would have to be done to say conclusively that a slower scan velocity is

beneficial: these are just a few test specimens and the results are relative to the other nominal levels of the process parameters.

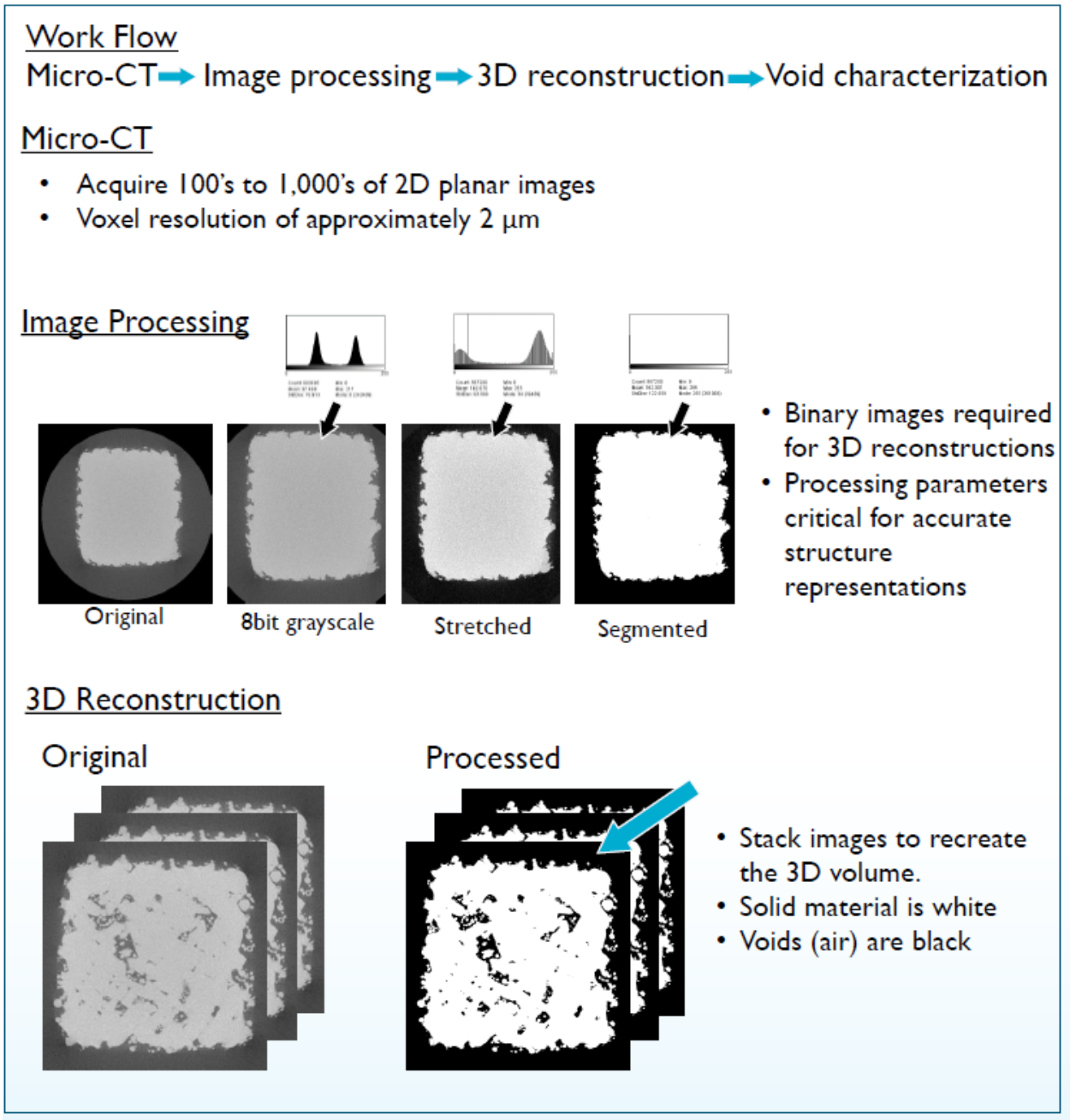

Figure 2.14. Workflow for thresholding, segmentation, and alignment of Gen 2 dogbone images during image processing.

Global Void Analysis

Minimum void volume: 27 voxels, ~151 µm^3

Equivalent spherical radius: 3.3 µm

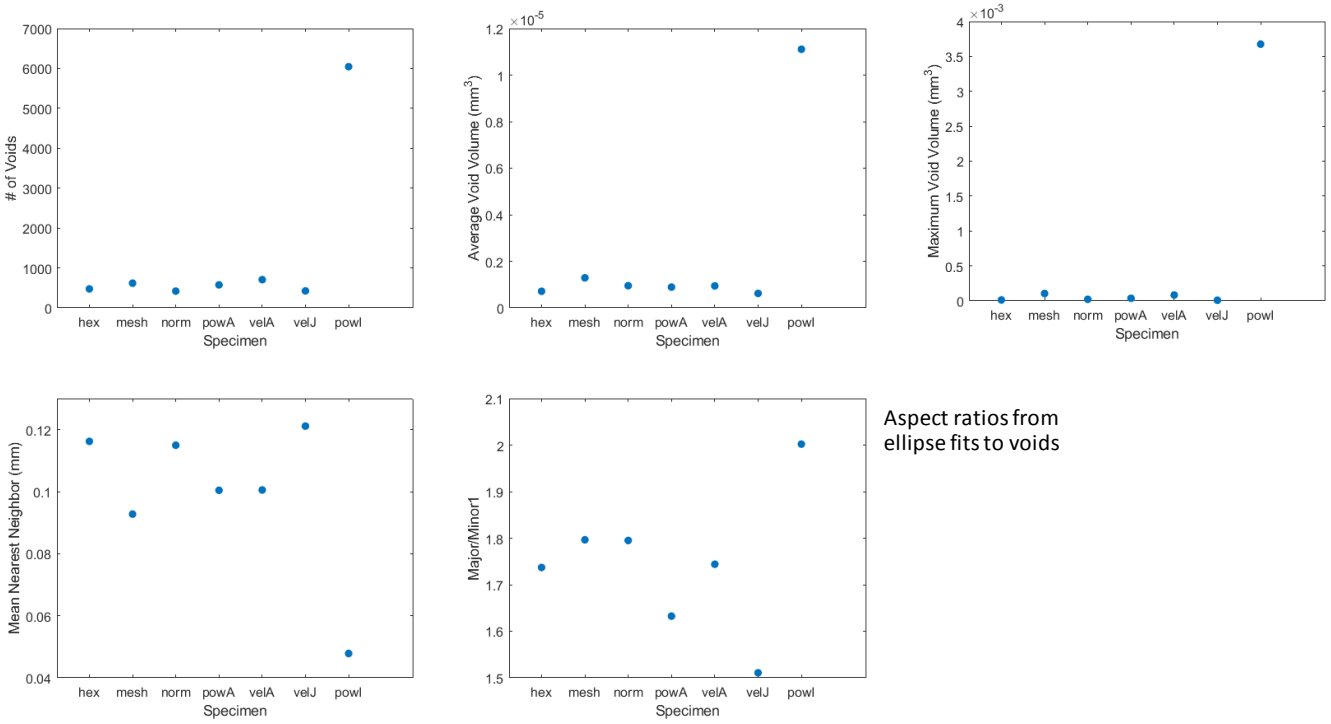

Aspect ratios from ellipse fits to voids

Figure 2.15. Plots of void metrics across all 7 Gen2 specimens

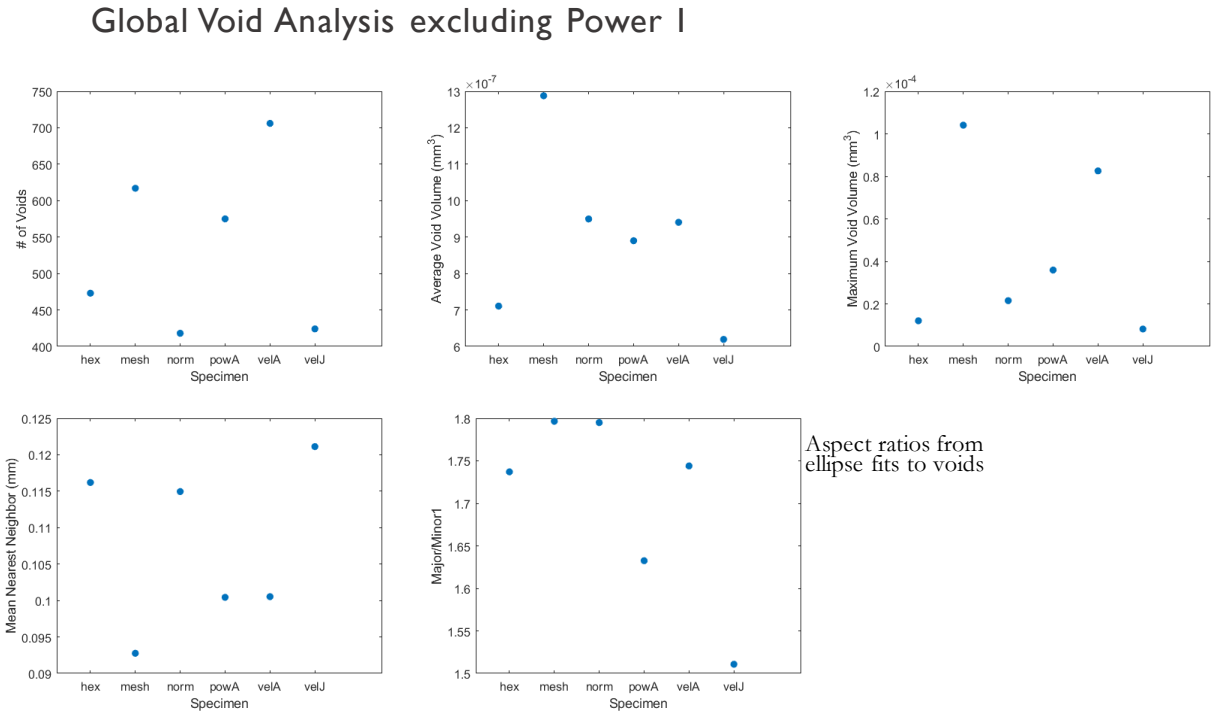

Figure 2.16. Plots of void metrics across six of the Gen2 specimens, excluding Power I

Figures 2.17 and 2.18 show plots of the void metrics relative to the material properties characterized for these specimens. The material properties of ductility, elongation, and ultimate tensile strength do not appear to exhibit a trend with respect to number of voids (Figure 2.17) or average void volume (Figure 2.18). This was also true for yield strength and modulus which are omitted for brevity. The material properties are not sensitive to the number or size of voids for these tensile bars.

A final set of analyses of the voids involved examination of two metrics describing the size and shape of the voids: Equivalent Spherical Diameter (ESD) and sphericity. ESD refers to the diameter of a sphere with a volume equivalent to a void. This is a way of normalizing differently shaped voids. Figure 2.19 shows the distribution of ESD values for the 6 tensile bars, excluding Power I. Figure 2.19 shows the raw histograms of ESD values corresponding to the actual voids in the specimens and also shows the corresponding fitted lognormal distributions, which are very similar across specimens. Figure 2.20 shows the same analysis for sphericity. Normally, a sphericity of 1 would indicate a perfect sphere. Note that we choose to plot (1-sphericity) instead on sphericity to show results on a lognormal scale. Thus, values close to zero in Figure 2.20 are nearly spherical and high values are not. Again, the histograms are similar across specimens. Finally, Figure 2.21 shows a scatterplot with material properties (UTS, elongation, and yield strength) plotted against the mean ESD and sphericity values. The Power I bar is shown in this plot. Based on the information in Figures 2.17-2.21, we conclude that differences in global porosity populations are minimal across most of the AM processing parameter space examined. Additionally, overall mechanical behavior is not strongly

correlated with the porosity information such as number of voids, void volume, ESD, or sphericity. Remember that these conclusions are based on a limited data set of seven tensile bars, so more specimens should be analyzed for stronger statistical conclusions.

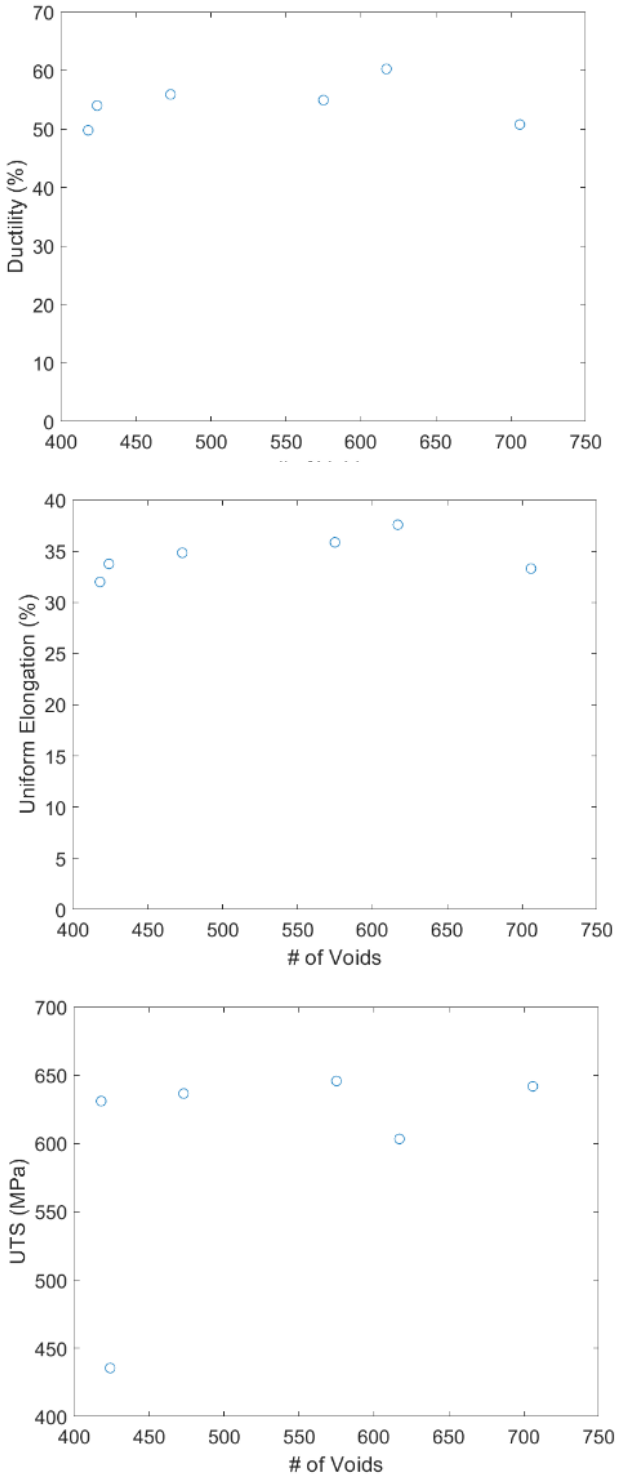

Figure 2.17. Mechanical Test Data vs Number of Voids, Gen 2 dogbones excluding Power I

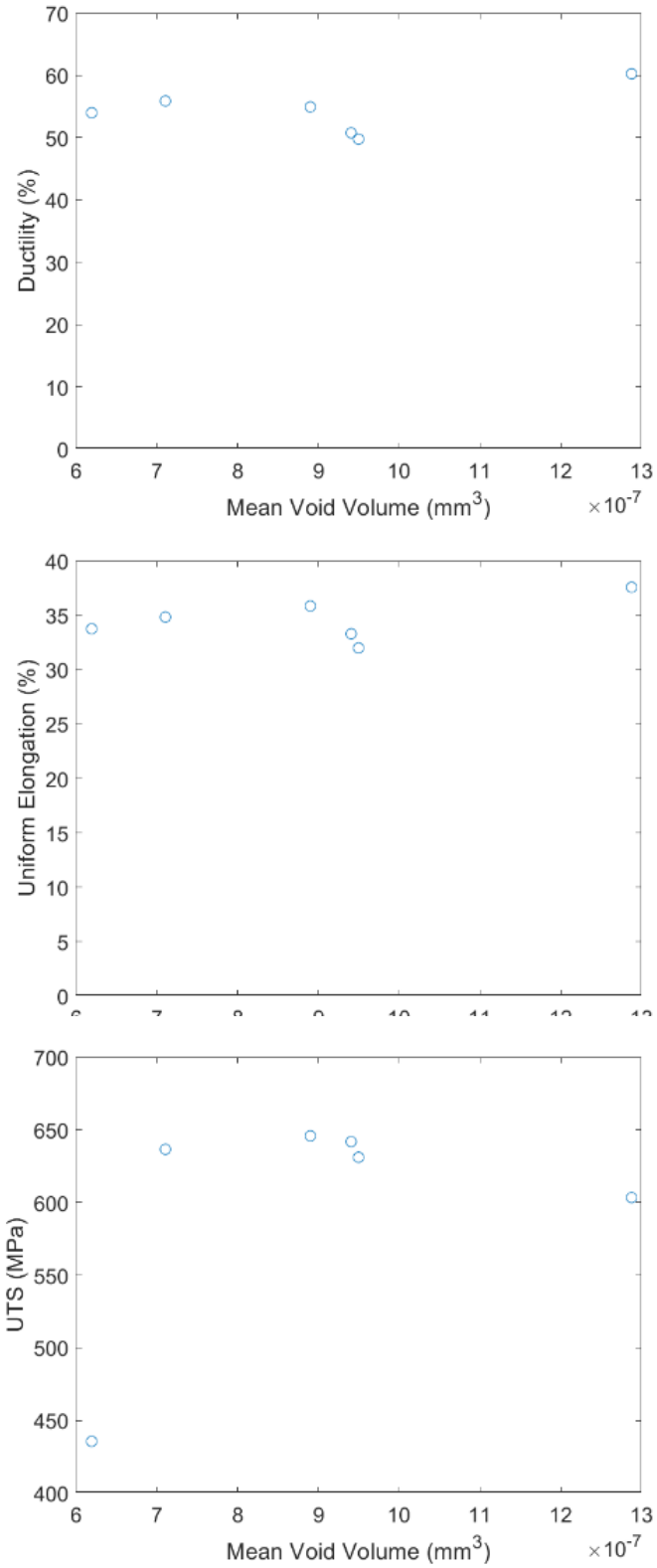

Figure 2.18. Mechanical Test Data vs Ave.Void Volume, Gen 2 dogbones excluding Power I

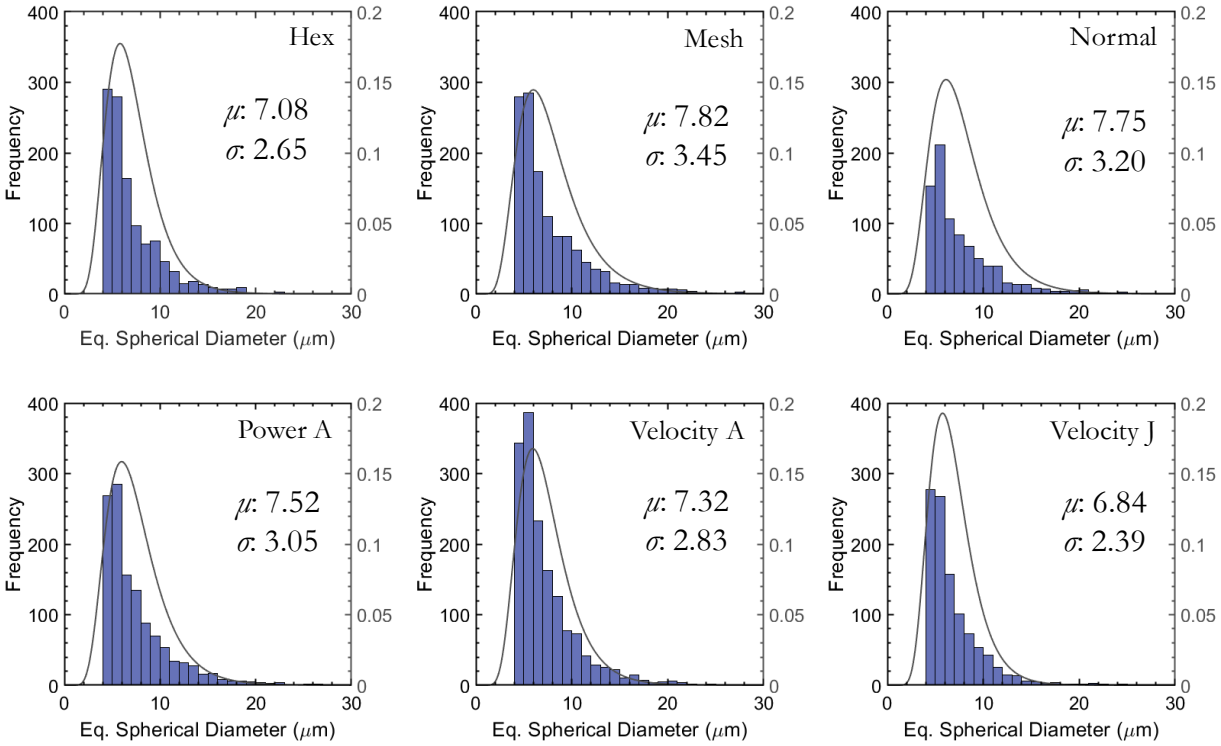

Figure 2.19. Distribution of Equivalent Spherical Diameter, Gen 2 dogbones excluding Power I

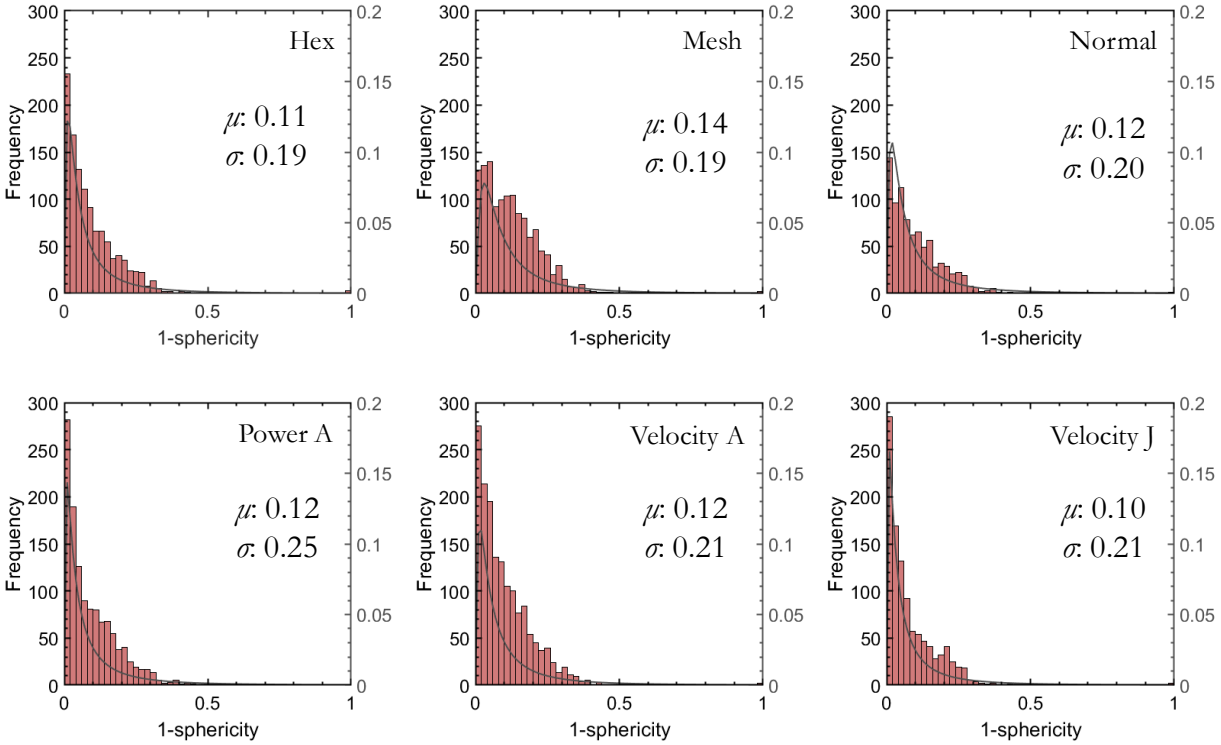

Figure 2.20. Distribution of (1-sphericity) for the Gen 2 dogbones excluding Power I

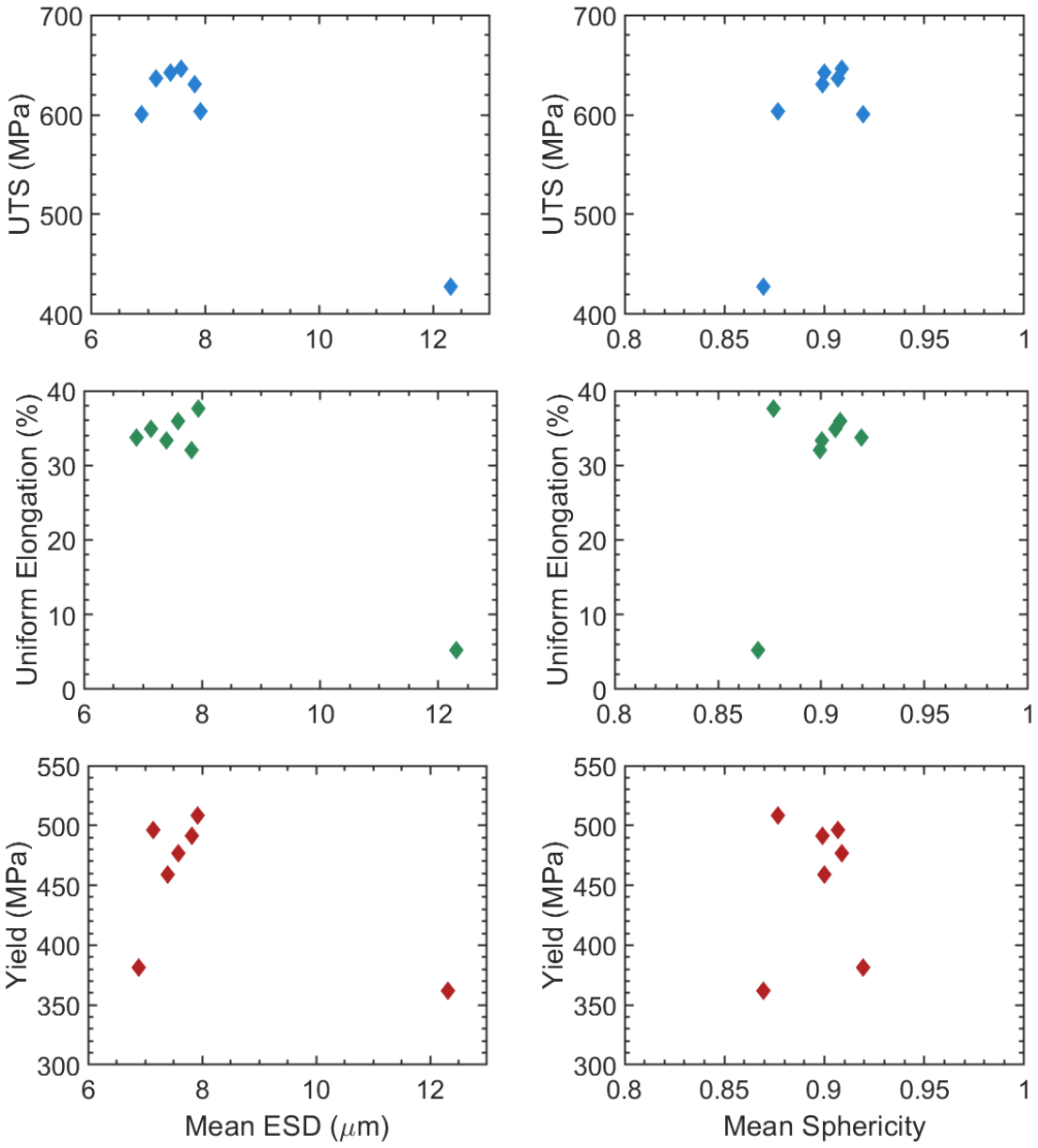

Figure 2.21. Material properties (UTS, Elongation, and Yield Strength) vs. Mean ESD and Mean Sphericity for the Gen 2 dogbones that had micro-CT scans. The outlier is the low power specimen, Power I.

Another analysis with the micro-CT data was to examine the pattern of voids with respect to the different scan patterns. Figure 2.22 shows the voids summarized in the Z-direction (looking down from the top of the tensile bar). It is clear that the majority of the voids occur near the edges of the cross section of the tensile bars. We have observed that more voids occur near the "crust" of additively made parts as shown in Figure 2.22. This figure does not support a large difference in the void pattern based

on the scan pattern. We believe that the larger band of the high-void region for the mesh pattern was because that particular specimen was bent, not due to a fundamental problem with the mesh pattern, but more testing and characterization are needed to verify this.

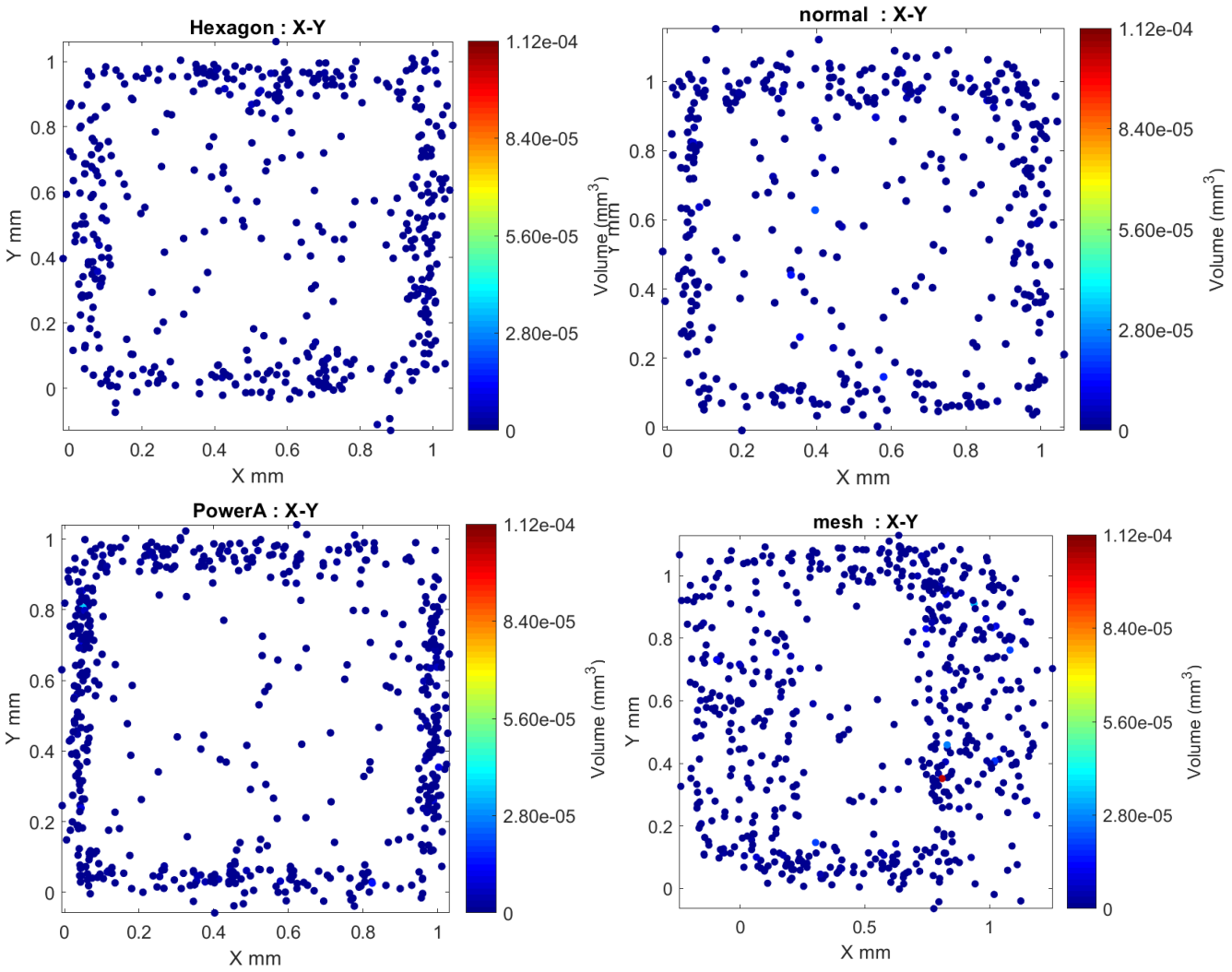

Figure 2.22. Patterns of voids for three scan patterns: hexagonal (both dogbones on the left were built with the hexagon pattern, the nominal hexagon and the power A specimen), the normal pattern (upper right), and the mesh pattern (lower right).

2.3. Powder Bed Process Map

The ProX200 machine was upgraded in the spring of 2018 with a new optics system for the laser. This was a significant upgrade and improved the laser focusing and thermal lensing offset issues that Bradley Jared identified. The new optics systems reduced the thermal lensing effects by an order of magnitude.

After the new optics system was installed, a team led by Josh Koepke embarked on a significant effort making a series of density cubes to identify an optimal process map for the new system. This section describes the experimental designs and analyses performed.

2.3.1. Density cubes

A series of ten plates with 316L stainless steel density cubes of were built. An example plate is shown in Figure 2.23. The cubes were 1cm on each side, with 24 cubes to a plate.

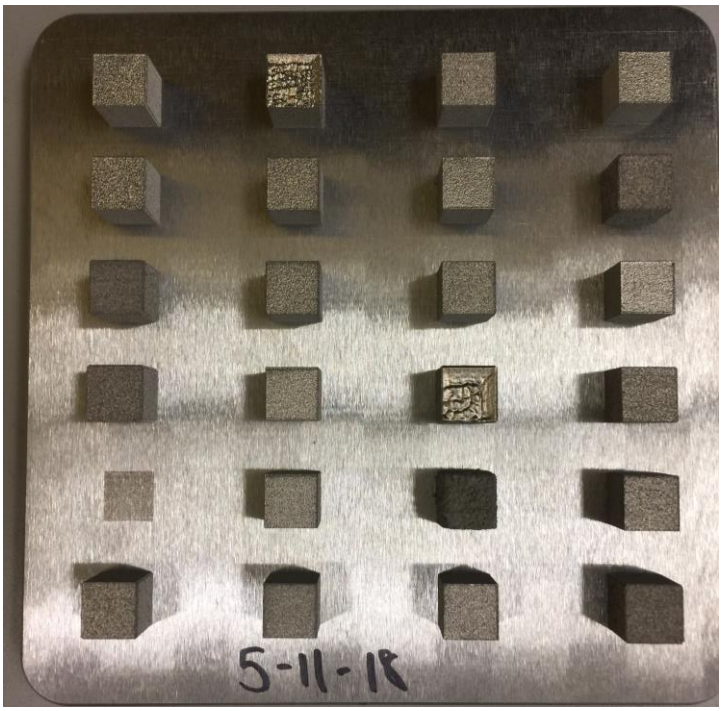

Figure 2.23. 316L density cubes

At the time of this writing, ten plates were printed and analyzed. All the plates involved variations of laser power and scan velocity. Plates 4, 5, and 9 involved a different powder size, and an additional variation was that some of the plates used 30 micron layer thickness while others used 40 micron layer thickness. The experimental designs for plates 1-4 are shown in Figure 2.24. Note that we did not do a broad parameter sweep equally over the space of laser power and scan velocity. Instead, we targeted samples around a line which we thought would give good performance. The laser power over the entire set of 10 plates varied from 10W to 240W. The scan velocity varied from 200 mm/s to 2800 mm/s. The density cubes initially built are

shown in blue dots in Figure 2.24. After this initial series of plates, we saw that cubes with higher volumetric energy density had better performance in terms of surface roughness and part density. Thus, the later plates were run at higher scan rates and higher power levels (in orange dots, higher scan rate plates were added subsequently).

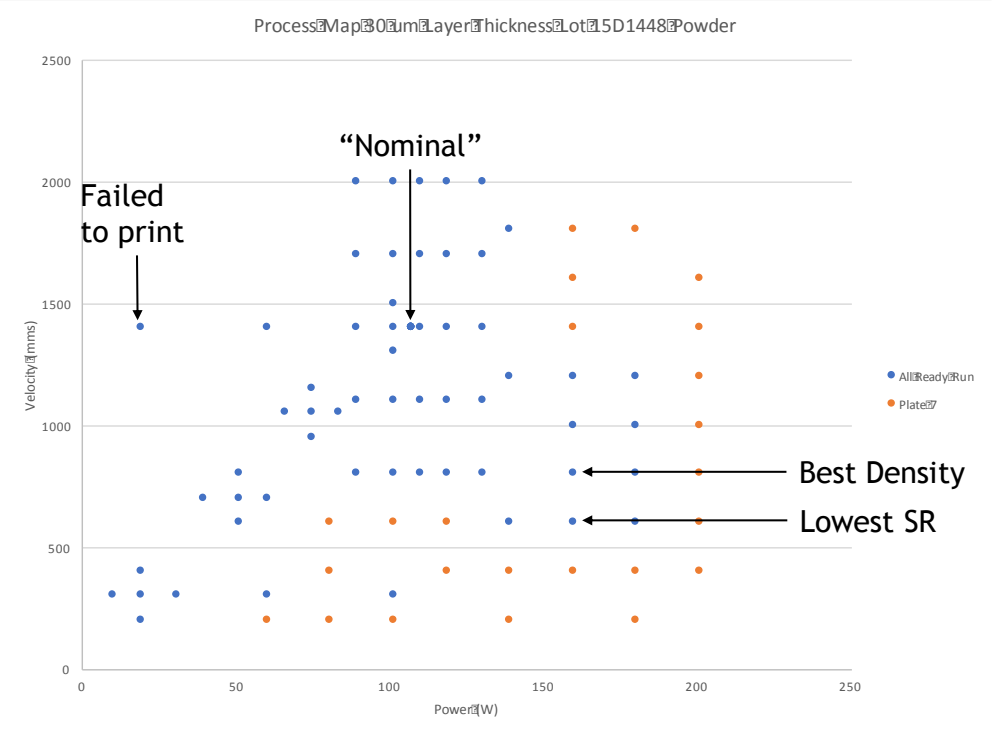

Figure 2.24. Parameter space exploration for 316L density cubes

Figure 2.25 shows scatterplots where the plates are colored with different symbols. This figure shows that plate 1 had the worst densities and plates 5, 9, and 10 had the best densities.

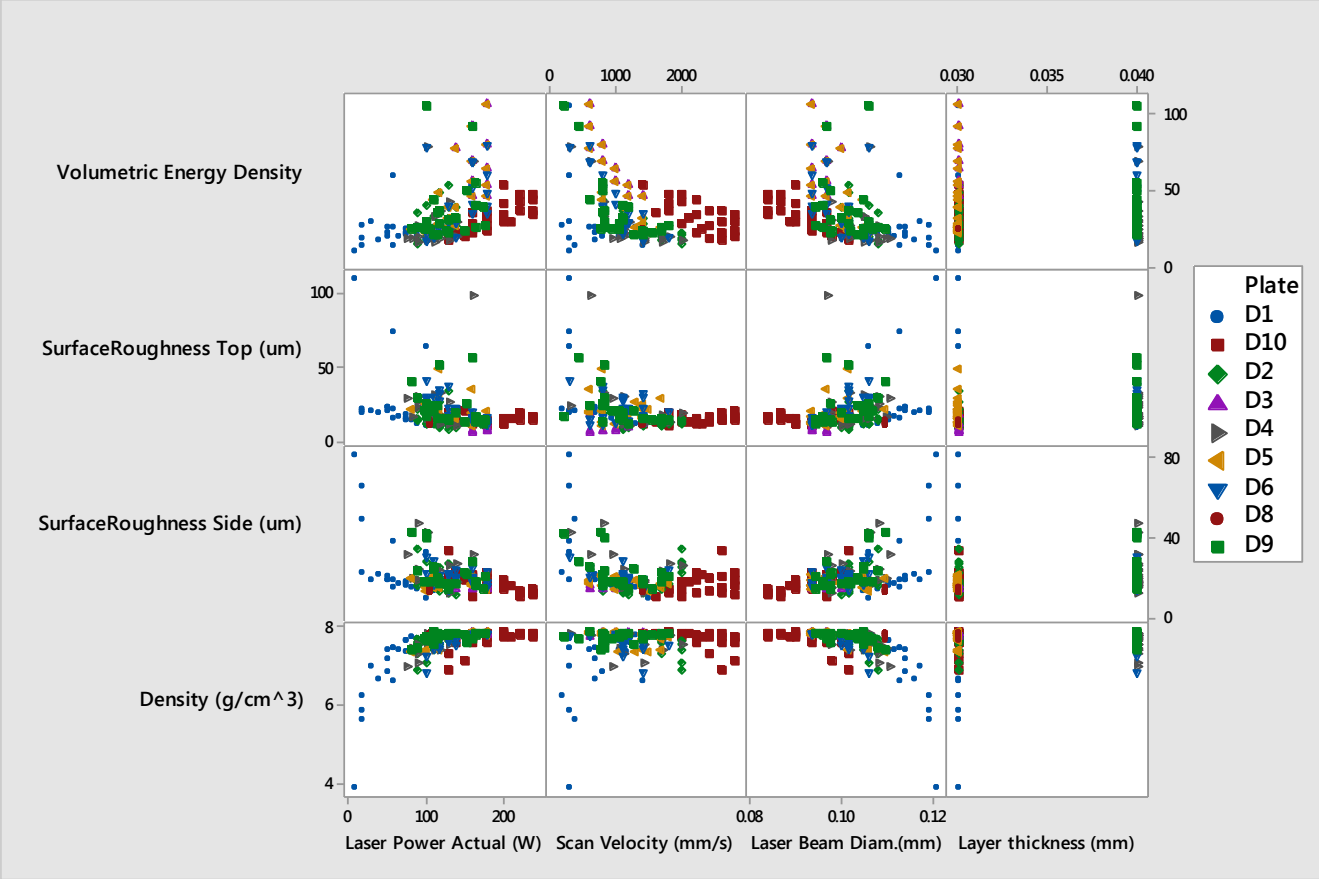

Figure 2.25 Scatterplots of the process settings (x-axis) and properties (y-axis) for the 316L Density Cubes

Table 2.4 shows correlations between the various material responses and the process settings. The correlations of density (g/cm^3) is the highest with respect to laser power (0.57), side surface roughness (-0.68), and laser beam diameter (-0.52) .

	Laser Power Actual (W)	*Scan Velocity (mms)*	*Laser Beam Diameter (mm)*	*Layer thickness (mm)*	*Volumetric Energy Density (VED)*	*Surface Roughness Top (um)*	*Surface Roughness Side (um)*	*Density (g/cm^3)*
Laser Power Actual (W)	1.00							
Scan Velocity (mms)	0.44	1.00						
Laser Beam Diameter (mm)	-0.97	-0.40	1.00					
Layer thickness (mm)	0.02	-0.24	-0.11	1.00				
Volumetric Energy Density (VED)	0.43	-0.48	-0.43	0.00	1.00			
SurfaceRoughness Top (um)	-0.25	-0.37	0.19	0.22	0.14	1.00		
SurfaceRoughness Side (um)	-0.38	-0.31	0.31	0.22	0.02	0.58	1.00	
Density (g/cm^3)	0.57	0.16	-0.52	0.09	0.33	-0.43	-0.68	1.00

Table 2.4. Correlations between attributes of 316L density cubes

The correlations indicate which variables are helpful to construct a regression model for prediction of density.

Consider a regression model as a function of laser power, scan velocity, and laser beam diameter. Layer thickness is not included because it does not have a significant effect on improving the regression. Further, we filtered the data: the full dataset has 201 individual density cubes. However, many of the cubes from the first few builds have very low volumetric energy density. These are visually seen, for example, by the blue dots representing density cubes on plate D1 in Figure 2.25. If we include these points, we get a better regression than is warranted. The set of 154 points containing only cubes with VED > 22 J/mm^3 is used for the regression modeling.

Initial examination showed that a linear regression as a function of the three process parameters was not very predictive: the R^2 value was only 28%. However, the regression equation with a second order term for laser power is:

```
Density (g/cm^3) = 3.823 + 0.01826 Laser Power Actual (W)
- 0.000013 Scan Velocity (mms)+ 22.83 Laser Beam Diameter(mm)
- 0.000042 Laser Power Actual (W)*Laser Power Actual (W)
```

This gives an R^2 value of 65%. All the terms are significant at a p-value of 0.05 except scan velocity. If we construct a regression model solely as a function of laser power, the R^2 value for a quadratic model is 60%. This indicates that when using the process parameters from these cubes to predict the density of the cubes, most of the variance of the density can be predicted with laser power alone: the other parameters do not add much additional prediction capability in the regression model.

Finally, we examined the differences in density with respect to two process inputs: the layer thickness (0.03 vs 0.04mm) and Powder Type (Type = 1 corresponds to Lot 15D1448 and Type = 2 corresponds to Lot 471836). Comparisons of the mean density for these populations were computed by one-way analysis of variance (ANOVA). The null hypothesis that the means are equal would strongly not be rejected in either case. For both of these parameters, the means were almost the same for each case as shown in Table 2.5, with all subset populations having a mean density close to 7.75 g/cm^3.

Layer Thickness (mm)	**Number of cubes**	**Mean Density**	**Std Dev. Density**	**95% Confidence interval on mean**
0.03	103	7.7461	0.2033	(7.7115, 7.7808)
0.04	51	7.7667	0.1090	(7.7175, 7.8159)
Powder Type	**Number of cubes**	**Mean Density**	**Std Dev. Density**	**95% Confidence interval on mean**
1	112	7.7525	0.1893	(7.7192, 7.7857)
2	42	7.7542	0.1439	(7.6999, 7.8086)

Table 2.5. Comparison of mean density (g/cm^3) across layer thickness and powder type.

Based on these density cubes, laser power is a strong predictor of density. Scan velocity does not have a strong influence. Laser power and beam diameter are strongly negatively correlated. The layer thickness and powder type do not show any influence in this set of cubes.

2.3.2. *Process Maps*

With the density cubes we have printed, we can start a process map characterization. Figure 2.26 shows density and surface roughness contours over the parameter space for cubes 1-3.

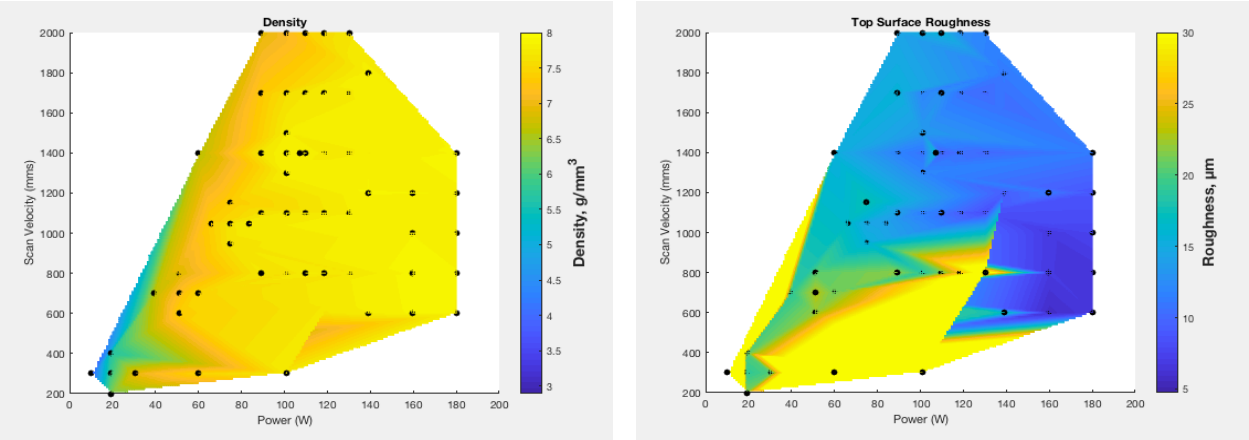

Figure 2.26. Contour maps of density and surface roughness over parameter space for density cubes from plates 1-3.

With some of the later data, we downselected the points with high volumetric energy density to narrow the region. It appears that a laser power setting of 60-180W and a scan velocity setting of 800-1200 mm/s are optimal with respect to both low surface roughness and high density. This is shown in Figure 2.27, where the "good" region in blue is circled in the lower contour plot.

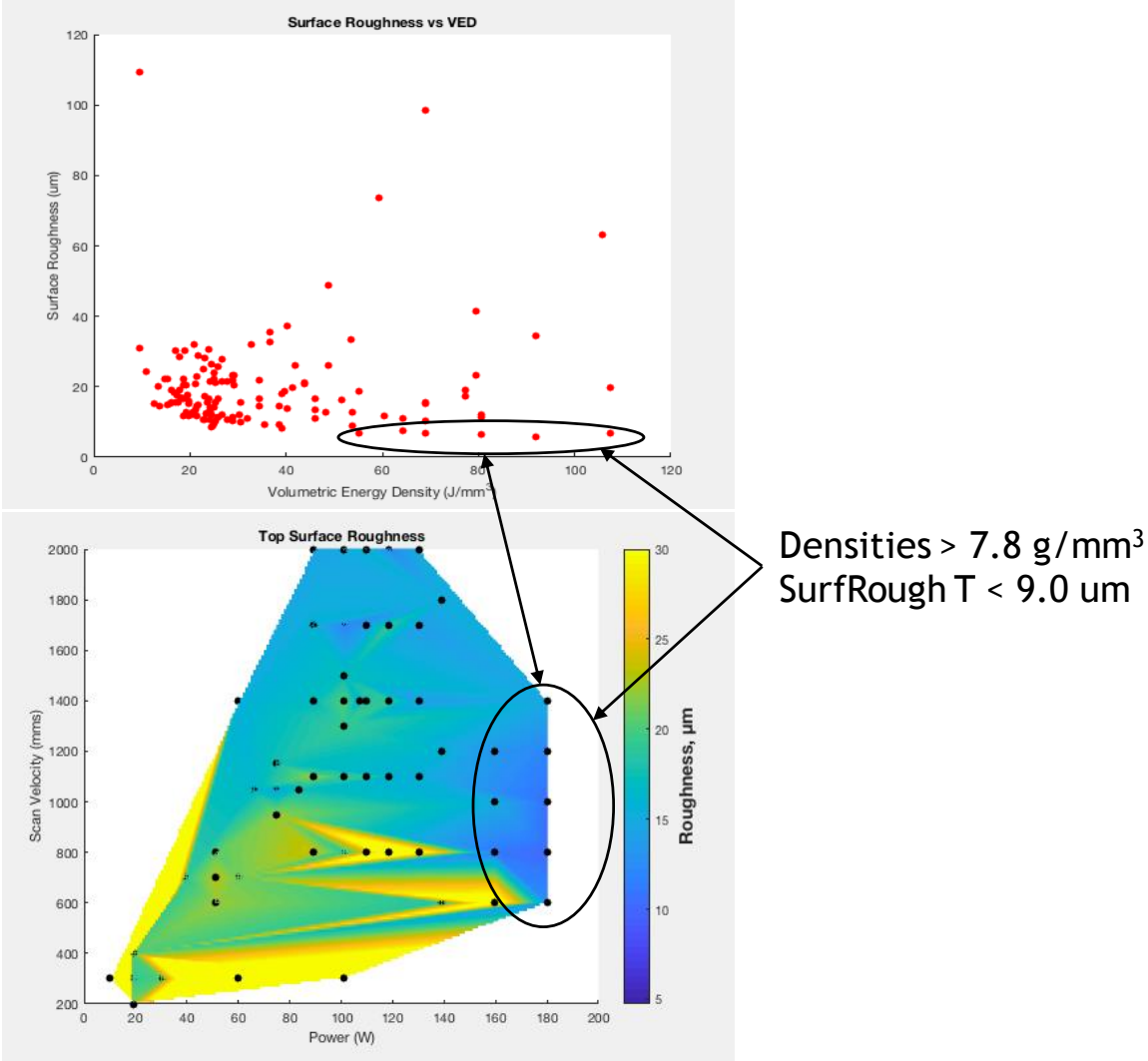

Figure 2.27. Optimal process settings over density cube plates 1-6 (plus focal plate), with high density and low surface roughness cubes highlighted in circled regions

2.4. Computational Simulation: Powder Bed Process to Properties

Part of the goal of the Born Qualified project is to develop capabilities to map AM process settings to the resulting properties of the parts built at those settings. Kyle Johnson has demonstrated an example of this with a Sierra model that models the laser powder bed process with coupled thermal and solid mechanics models.

This work modeled the gauge section of a tensile dogbone. The goal was to develop a full part-scale continuum model that can model the powder bed process to address the P-S-P-P map as shown in Figure 2.28.

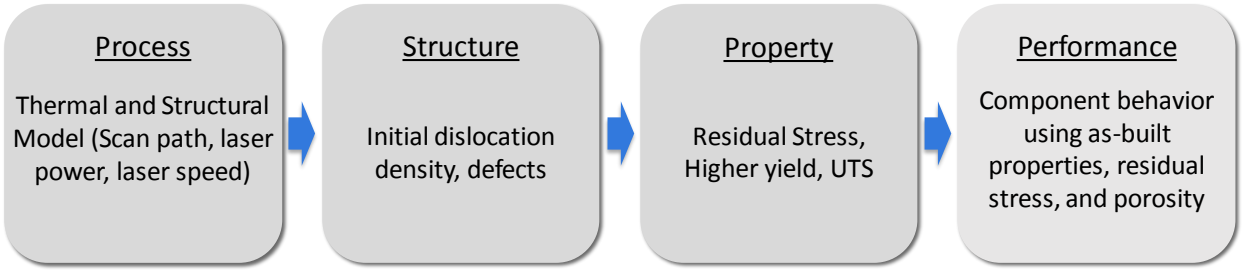

Figure 2.28. P-S-P-P mapping for the gauge section of a PB dogbone

The thermal model is in Aria and the solid mechanics model in Adagio. The overall computational framework using Sierra is shown in Figure 2.29 (thermal) and 2.30 (solid mechanics). The thermal history is used by the solid mechanics simulation in a one-way coupling. A Bammann-Chiesa-Johnson (BCJ) material model is used, which is a temperature and history-dependent viscoplastic model. The material model state variables evolve due to thermo-mechanical loading, and hardening, recovery, and recrystallization are tracked. Note that the BCJ model has been calibrated to wrought material. Porosity is included by mapping the porosity distribution onto the mesh.

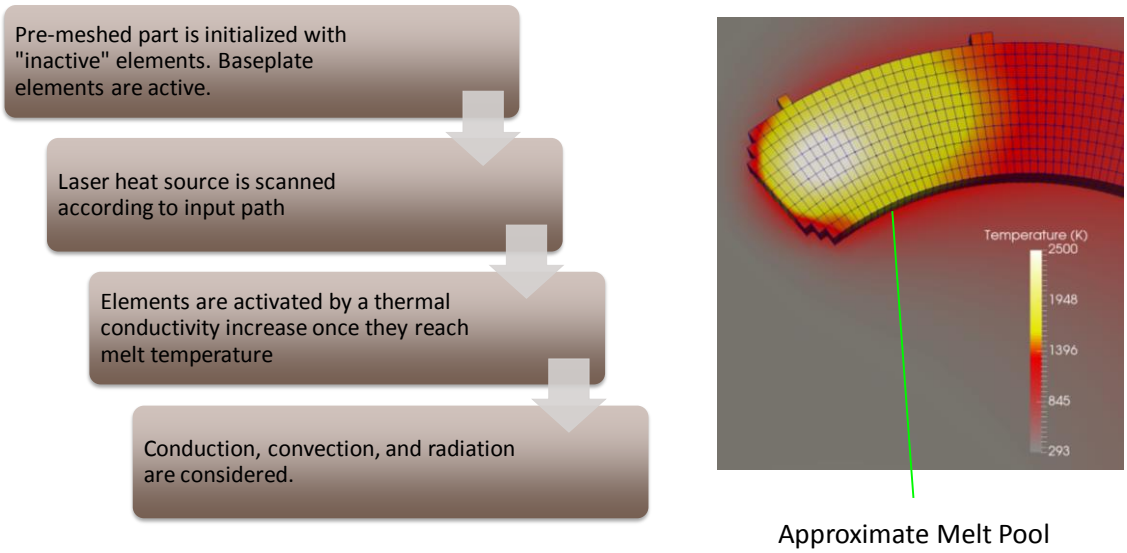

Figure 2.29. Thermal Model for simulation of Powder Bed AM Process in Aria.

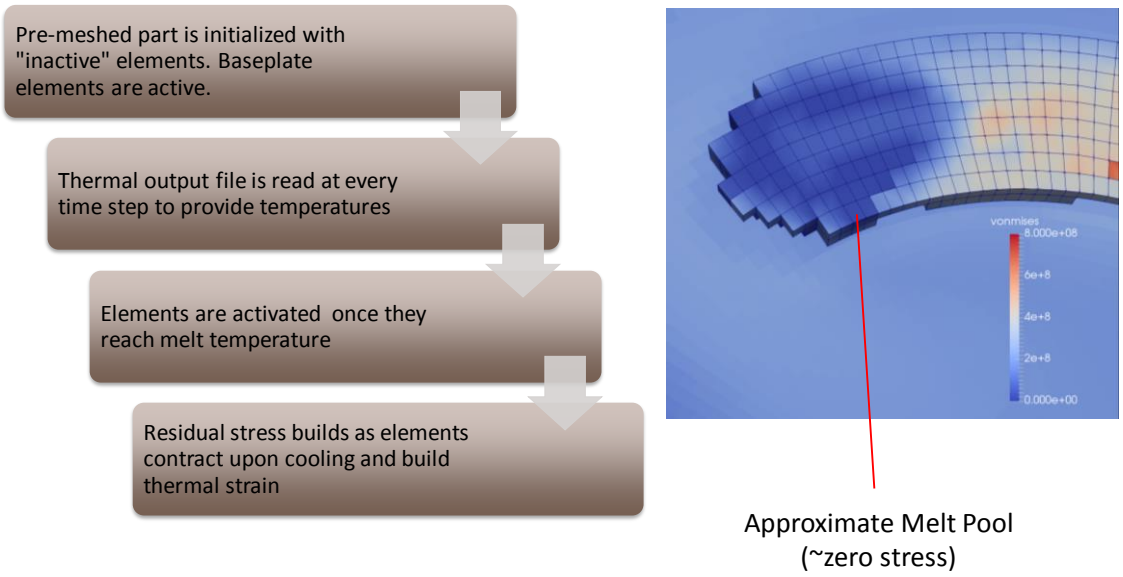

Figure 2.30. Solid Mechanics model for simulation of Powder Bed AM Process in Adagio.

The results of these coupled simulations show that significant compressive and tensile residual stresses (up to 400MPa) remain in the dogbone after the part is built. To understand the variability in the results due to variability in the process, we ran a simple, full factorial experiment, varying two process parameters: laser power and scan velocity. This simple study is shown in Table 2.6. We chose this simple 3x3 study because it was similar to some of the experimental runs that were performed on the ProX200 machine, and thus can provide both a main effects sensitivity analysis as well as basis for some initial validation of the simulation model.

	Laser Power (W)		
Scan Velocity (m/s)	100	110	125
1.05			
1.4			
1.75			

Table 2.6. Design of experiments for simulation runs modeling the gauge section of the powder-bed dogbone

Figure 2.31 shows scatterplots of data from the 9 runs overlaid with a linear trend line. These scatterplots show how the maximum temperature, the von Mises stress, and density vary with respect to laser power and scan velocity. Laser power is positively correlated to maximum temperature and density. Scan velocity is negatively correlated with temperature and density, and positively correlated with von Mises stress. Figure 2.32 shows main effects plots, which involve the mean response value (where response = temperature, density, or von Mises stress) at the various levels of laser power and scan velocity. These plots indicate that these responses have a higher sensitivity to scan velocity than to laser power. Note, however, that such sensitivity analyses are highly dependent on the range of the input variables. Scan velocity was varied over quite a large range: from 1.05 to 1.75 m/s. If the range had been half that, the results would likely show a greater sensitivity to laser power, especially for density.

Figure 2.31. Scatterplots of results from the 9 PB simulation runs with inputs on X-axes and outputs on the Y-axes.

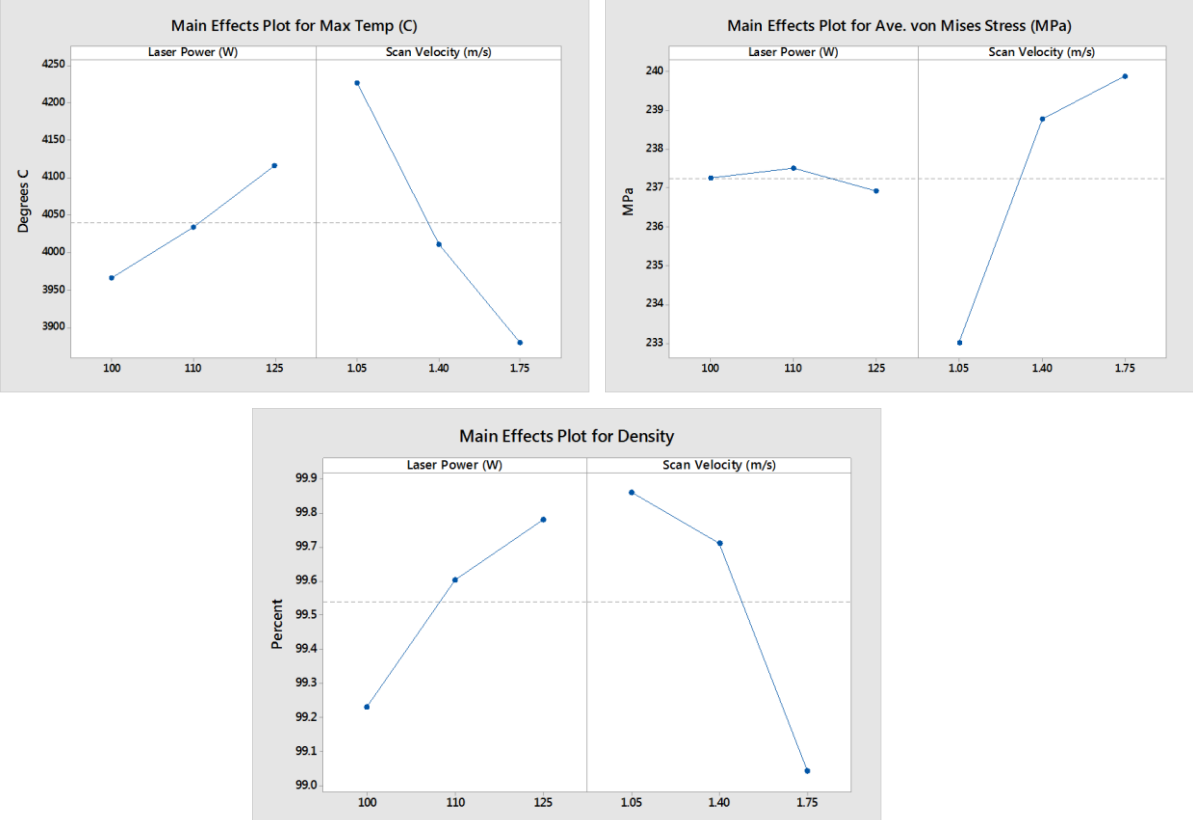

Figure 2.32. Main effects analyses of the 9 simulation runs with respect to maximum temperature, von Mises stress, and density.

Finally, Figure 2.33 shows a comparison of the yield strength predictions from the model with those from experimental data generated by making the dogbones on the ProX200 machine. Note that the yield strength from the experiments was estimated from the published modulus (center) and the unloading modulus (right). This chart shows that the simulation model under-predicts yield strength by ~50MPa when compared to the experimental yield strength as calculated from the published modulus. One contributing factor to this underprediction is the fact that the BCJ material model was calibrated to wrought material, not additively manufactured material. Another possible cause of the discrepancy in yield stress could be model-form error, meaning there could be phenomena present in the AM process that are not captured by the constitutive model in its current form. This is something that will be addressed in future work.

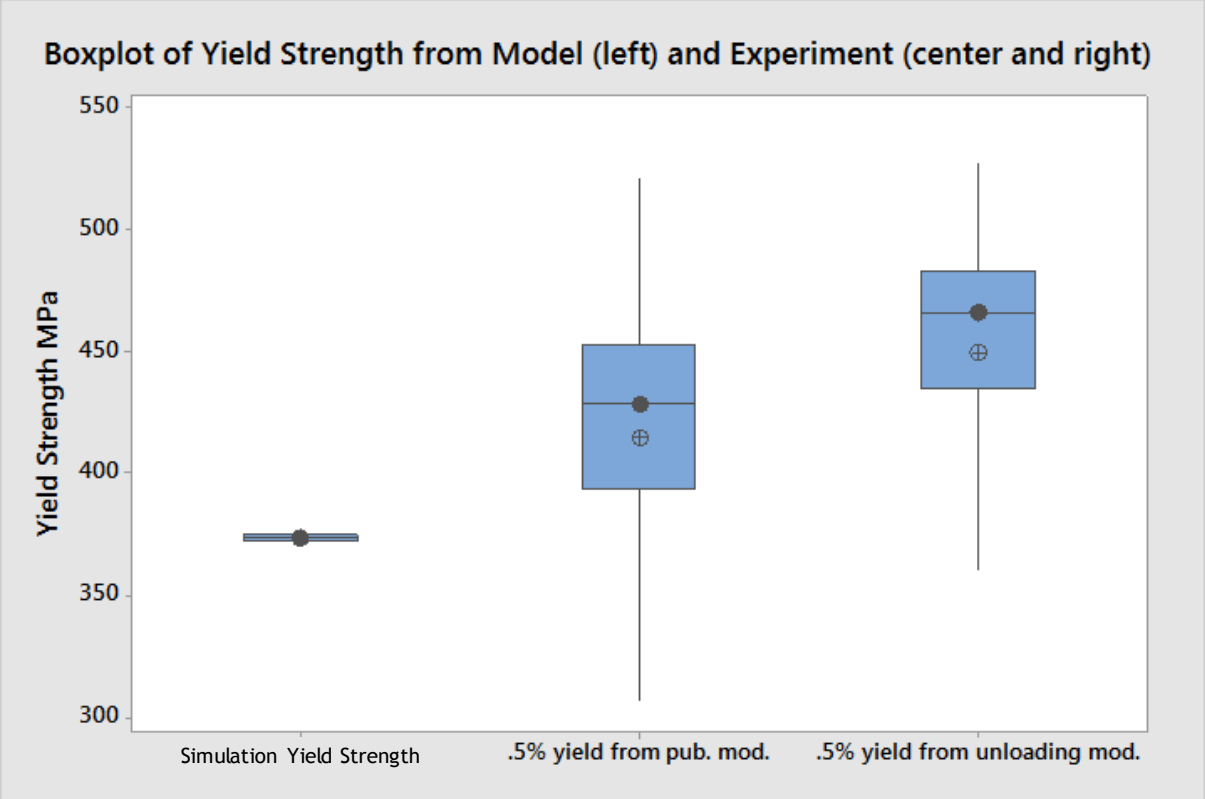

Figure 2.33. Comparison of simulation predictions of yield strength (left column) with tensile test results from dogbones made on the ProX200 machine (center and right).

3. LENS

Laser Engineered Net Shaping (LENS) refers to a process where metal powder is injected into a molten pool created by a laser beam. Similar to powder bed, it uses laser melting and metal powder. However, in contrast to a laser sweeping over a plate of powder, the metal powder is supplied through a deposition head in LENS, and the laser beam typically travels through the center of the head.

3.1. Demonstrator 1

To develop some understanding of the LENS meltpool, four "demonstrators" of 316L stainless steel were printed on the LENS machine, where each demonstrator is a plate with 10 lines as shown in Figure 3.1. The four plates of 10 lines each were printed at 400 and 600 mm/min, and without and with powder. Data from a two-color thermal imaging pyrometer system called ThermalViz was collected for each line. An example of the snapshot of the image from the ThermalViz system is shown in Figure 3.2 below.

Figure 3.1. One of the four LENS demonstrator sets. This plate was printed at 600 mm/minute with powder.

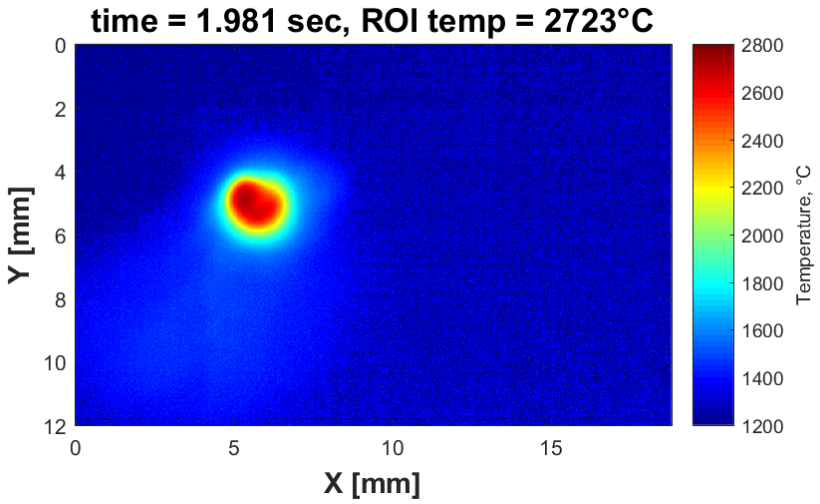

Figure 3.2. Example melt pool image from the ThermalViz system for LENS

The typical line took over three seconds to produce. This study examined the distribution of peak temperature at 1 and 2 seconds. We focused only on data from the two plates at 400 mm/min since some data was missing from 600 mm/min sets. Figures 3.3 and 3.4 show the distributions of the data at 1 second and 2 seconds, respectively. Plate 1 had no powder (NP) and Plate 2 had powder (P). Plate 2 with powder resulted in higher peak temperatures at both times.

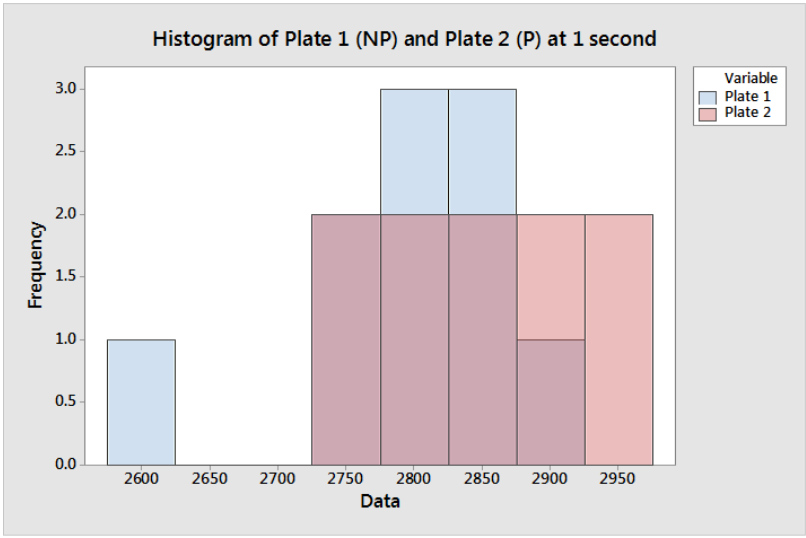

Figure 3.3. Peak temperatures of plates 1 (400mm/min, no powder) and 2 (400 mm/min, with powder) at 1 second.

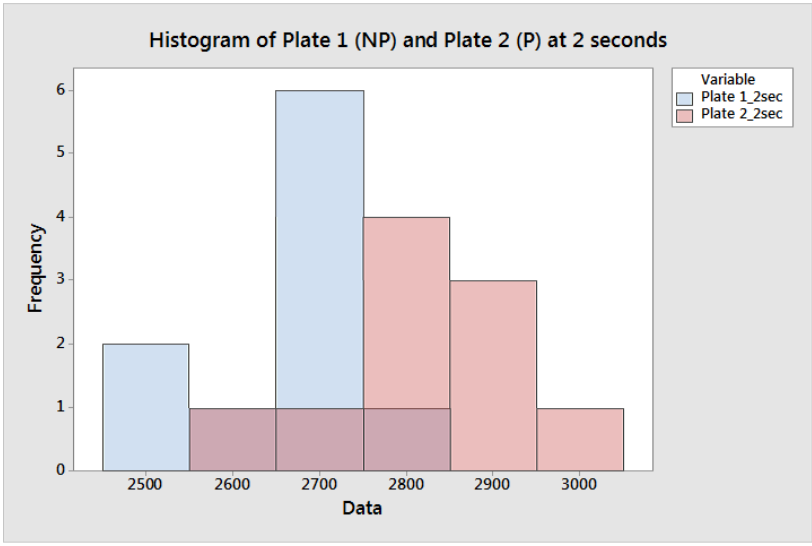

Figure 3.4. Peak temperatures of plates 1 (400mm/min, no powder) and 2 (400 mm/min, with powder) at 2 seconds.

Figure 3.5 shows a main effects plot, comparing the mean temperatures under the different conditions. Figure 3.5 shows that the mean temperature is statistically significantly different (lower) for plate 1 (NP) than for plate 2 (P). The mean temperature for plate 1 is 2729 °C, but is 2836 °C for plate 2. So the powder raised the temperature by more than 100 degrees. The p-value is 0.002, meaning that we would reject the null hypothesis that the means are the same across plates 1 and 2: they are different. The mean temperatures at the two times (averaged across the plates) are also different. The temperature is higher at 1 second than at 2 seconds. Finally, Figure 3.6 shows an interaction plot. This figure shows that the drop in temperature at 2 seconds is more pronounced for the no powder plate.

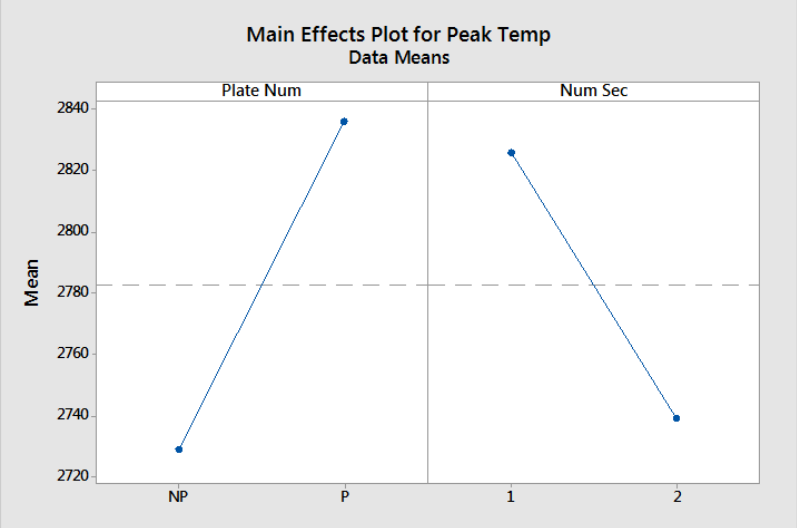

Figure 3.5. Main effects plot for peak temperatures showing the mean peak temperature with no powder or powder (left side) and at 1 second or 2 seconds (right side).

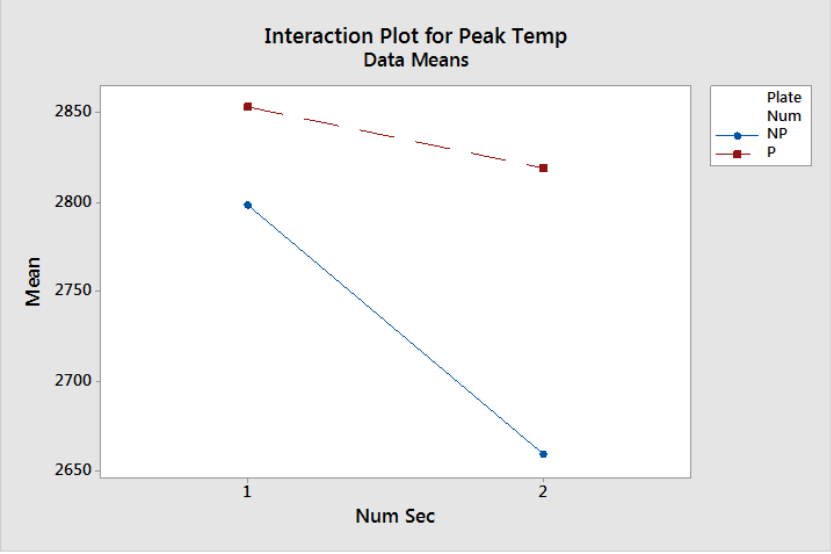

Figure 3.6. Interaction plot showing the temperature variation both in plates (different colored lines) and time (x-axis).

3.2. Build orientation

A study was performed to understand the effects of build orientation with respect to LENS. Three different build orientations were printed and tensile bars were machined out of the blocks for high throughput tensile testing. Each of the three build orientations had 2 replicate builds printed, e.g. Build 1A and 1B, 2A and 2B, and 3A and 3B. The orientations are shown in Figure 3.7.

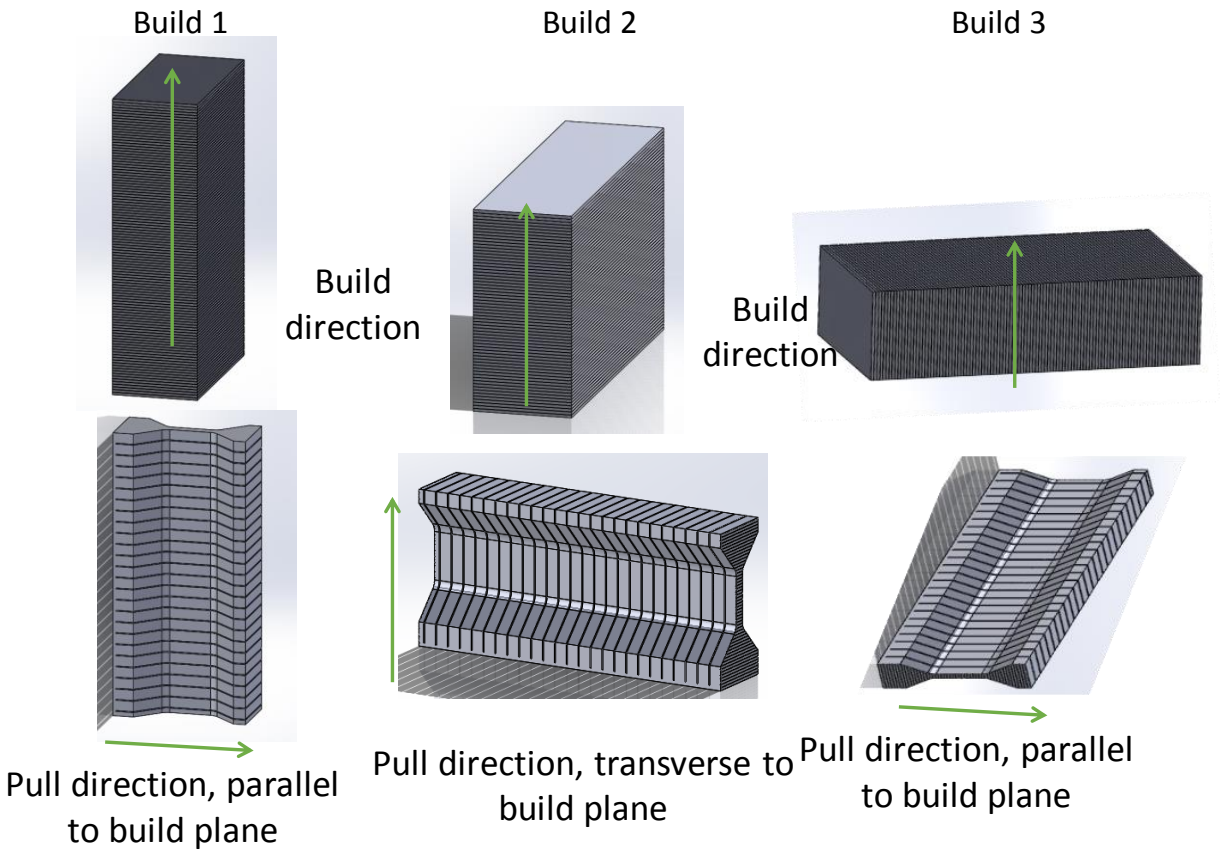

Figure 3.7. Three build orientations examined by LENS study, Oct. 2017

The builds were created with the following process conditions: Platen temperature of 30 °C, Powder Feeder Voltage of 3.5V, Laser Power of 450W, Table Feedrate of 600 mm/min, and Layer height of 0.25 mm. Figure 3.8 shows the stress-strain curves for the six builds. Table 3.1 shows the summary statistics from the builds. These are average properties over the number of dogbones produced in each build. Typically, there were 28 valid dogbones per build, but often the number was less due to various issues.

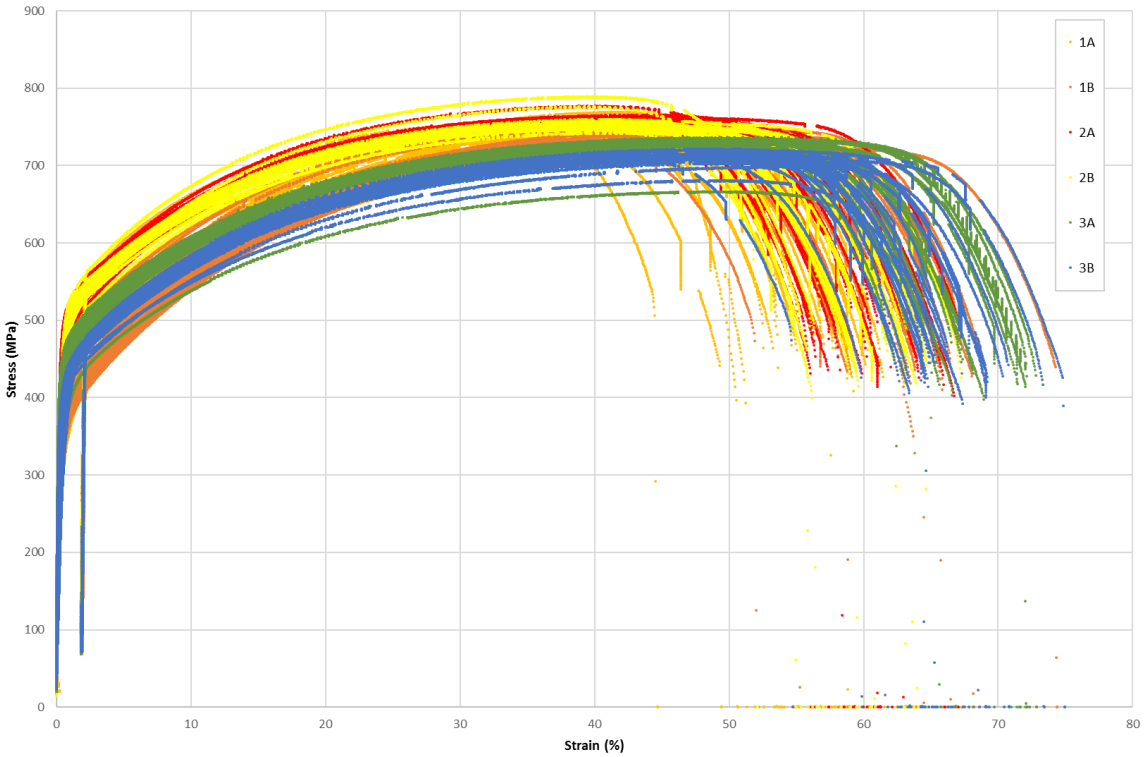

Figure 3.8. Stress-strain data from the 6 LENS builds of tensile specimens at 3 orientations

Sample Set		Unloading Modulus (GPa)	Yield from Unloading Modulus (MPa)	Nominal Unloading Modulus (GPa)	Yield from Nominal Unloading Modulus (MPa)	Unloading Yield from Published Modulus (MPa)	UTS (MPa)	Ductility (%)	Work Hardening Rate (GPa)	Measured Area (mm)
1A	Average	156	384	125	309	380	737	55.9	1.730	0.802
	St. Dev.	14	39	14	43	39	17	4.4	0.077	0.036
	Standard Error	3	8	3	9	8	3	0.9	0.015	0.007
1B	Average	153	371	149	362	365	733	62.8	1.613	0.977
	St. Dev.	12	25	11	28	24	10	4.7	0.062	0.020
	Standard Error	2	5	2	5	4	2	0.9	0.011	0.004
2A	Average	154	498	148	479	491	759	60.6	1.483	0.962
	St. Dev.	10	19	10	19	23	6	3.3	0.102	0.004
	Standard Error	2	4	2	4	5	1	0.7	0.021	0.001
2B	Average	156	493	148	469	487	754	60.2	1.455	0.951
	St. Dev.	10	14	10	12	16	9	3.7	0.117	0.005
	Standard Error	2	3	2	2	3	2	0.7	0.022	0.001
3A	Average	159	441	149	411	435	728	67.8	0.000	0.934
	St. Dev.	16	28	17	28	32	14	3.3	0.000	0.023
	Standard Error	3	6	4	6	7	3	0.7	0.000	0.005
3B	Average	152	413	142	386	406	711	65.9	1.483	0.934
	St. Dev.	13	20	13	22	25	8	4.0	0.080	0.012
	Standard Error	2	4	3	4	5	2	0.8	0.015	0.002

Table 3.1. Summary properties from the 6 LENS builds

As shown in Table 3.1, the unloading Modulus is consistent across all samples around 155 GPa. The yield stress is consistent within subsets (A,B), but varies between the builds, with Build 2 having the highest yield stress, followed by Build 3 then Build 1. Ultimate tensile strength follows this trend as well. The ductility is larger in Build 3 than in Builds 1 and 2. Build 1A has significantly less cross-sectional area than the remaining builds.

Figure 3.9 shows the yield stress data from all the specimens plotted according to a two-parameter Weibull distribution. The separation in yield strength distributions across the three build orientations is clearly seen, as well as the similarity in the (A, B) builds within a build orientation. Note that some of the data sets are not very well fit with a Weibull distribution, especially Build 1A and 1B.

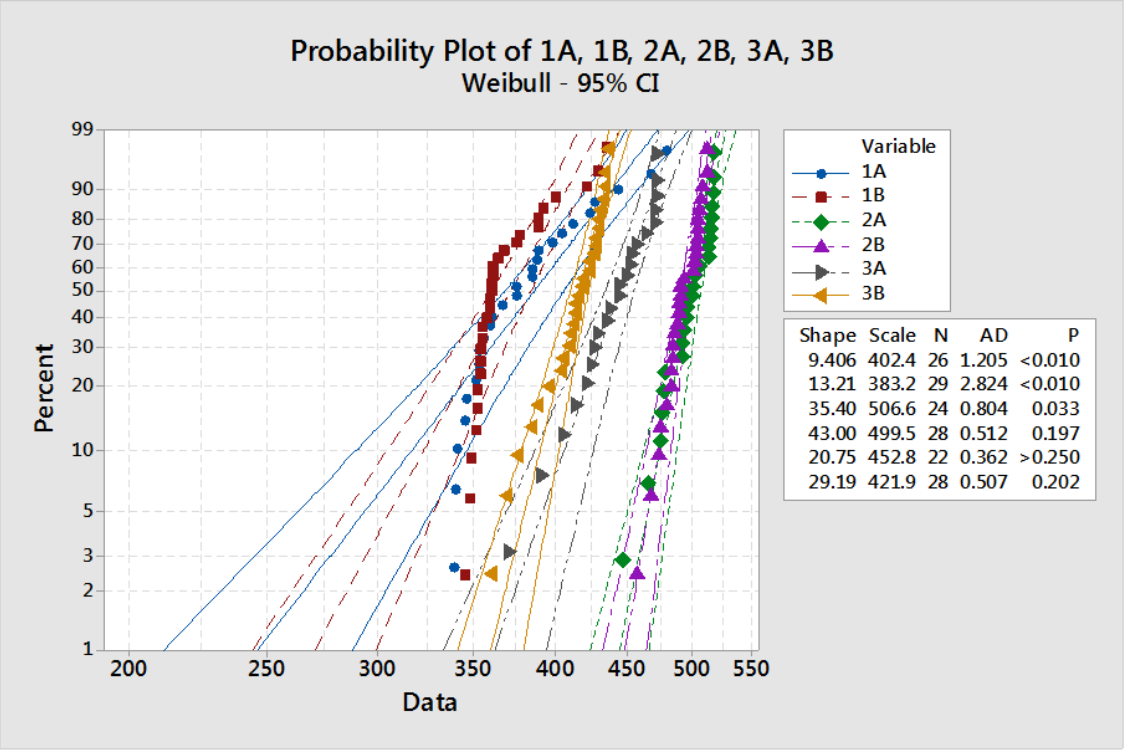

Figure 3.9. Weibull fits of Yield Strength (GPa) for different build orientations, LENS

Performing statistical tests for the hypothesis of the same mean yield strength across builds shows that we would strongly reject the null hypothesis that the mean yield strength is the same across Builds 1, 2, and 3. For example, the t-test value for mean yield strength of the builds being the same is 2.01 at the alpha = 0.05 level (e.g. if the t-test result is between -2.01 and 2.01, we accept the null hypothesis). The t-test for builds 1A and 3A is -5.66 and for builds 1A and 2A is -12.83. These values are very far away from the t-test bounds. Thus, we conclude that build orientation has a statistically significant effect on yield strength of stainless steel tensile bars produced in LENS.

4. DIRECT WRITE

4.1. Insulator ring

The Direct Write process is used to print ceramics and polymer-ceramic composites. Direct Write was used to print several types of sintered alumina parts in Born Qualified. The exemplar of interest was an insulator ring, as shown in Figure 4.1.

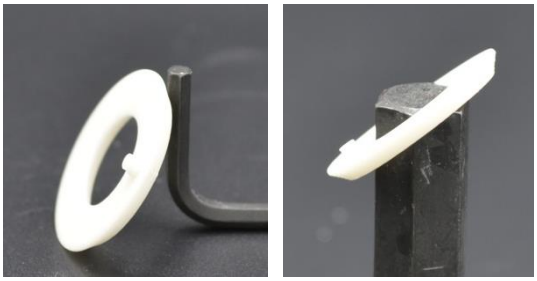

Figure 4.1 AM Alumina Insulator Ring

We gathered extensive data sets for the insulator ring. In particular, we have particle size distributions for the alumina powder used in the feedstock as well as rheological properties of the feedstock. We have process data from the Direct Write machine, specifically (x,y,z) spatial locations of the build path as well as the platen temperature, the extrusion temperature, and the syringe force (pressure) at the extrusion tip where the material is released onto the part. Finally, we have micro CT data for a few rings, both in the "green state" and CT data from the final sintered part.

The ultimate goal of the data analysis is to relate deposition instabilities to machine toolpath to part defects to identify and threshold acceptable vs. unallowable defects. Toward that goal, we developed scripts to identify large voids in the TIFF stacks from the CT scans and correlate those with the process data. An example of a TIFF image for the insulator ring is shown in Figure 4.2.

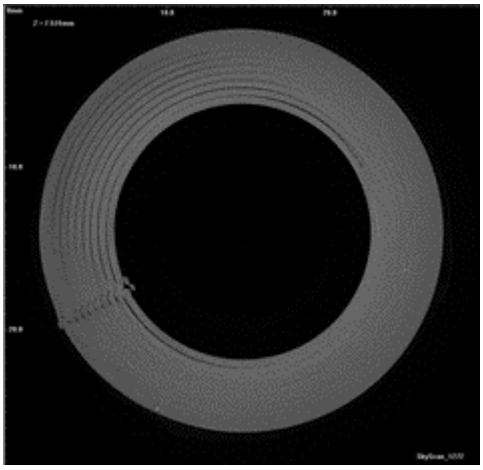

Figure 4.2. Example CT slice (slice in z-direction, showing x-y plane in image) from green state insulator ring

We developed scripts to take the process data (x, y, and z locations, plate and extrusion temperatures and pressure) and slice the data in z-direction. For each z-slice, we

calculated the average pressure and other statistics per slice. We also developed scripts to identify large voids in TIFF stacks from CT scans. These are the points highlighted in blue on the ring in Figure 4.3. Note this is a challenging data extraction problem, because a lot of the "black lines" on the CT image are an artifact of the toolpath which goes around in a circular pattern as shown in Figure 4.4. Our script did not take the toolpath as voids, only bigger voids.

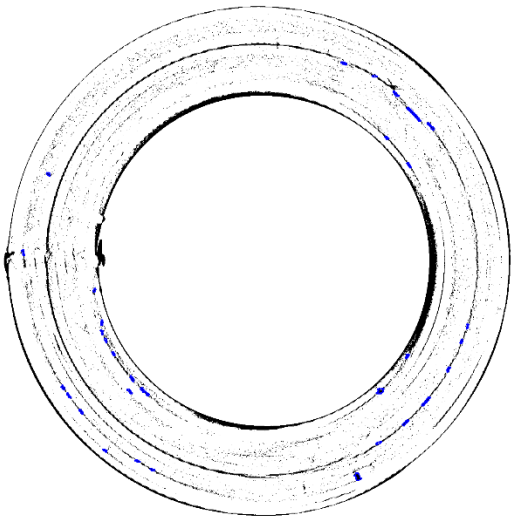

Figure 4.3. CT image after segmentation and thresholding, where large voids are highlighted in blue.

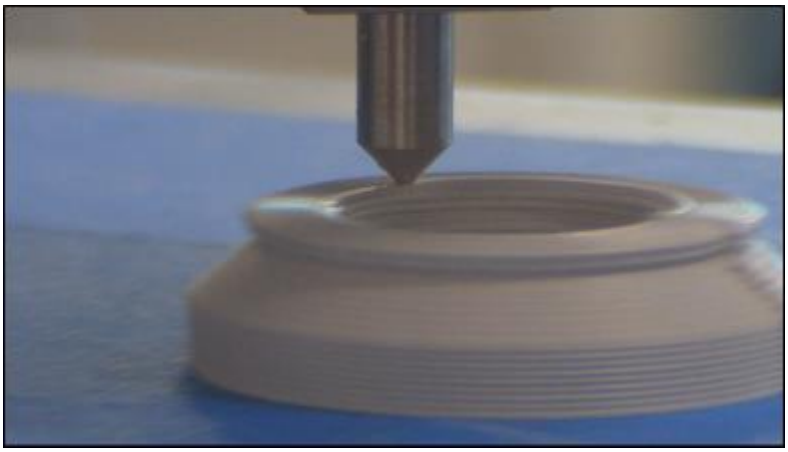

Figure 4.4. Direct Write printing process for composite polymer-ceramic

The results are shown in Figure 4.5. This preliminary analysis indicates that the number of voids increases in z-direction (e.g. as you build up the part) but the pressure decreases in the z-direction.

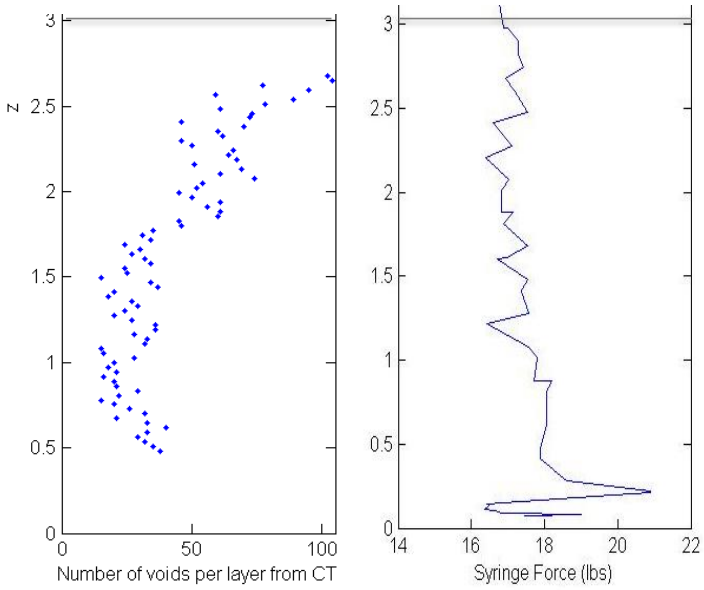

Figure 4.5. Results from insulator ring number 7760, with voids from green state CT (on left) as a function of z-layer and syringe force on right from aggregated process data.

4.2. Demonstrator cubes

More unit-level testing for the direct write process was performed with the printing of cubes. These cubes are "demonstrators" illustrating size effects that may occur in printing of alumina at various scales. The cubes are shown in Figure 4.6. The largest cubes are approximately 1.2 cm high.

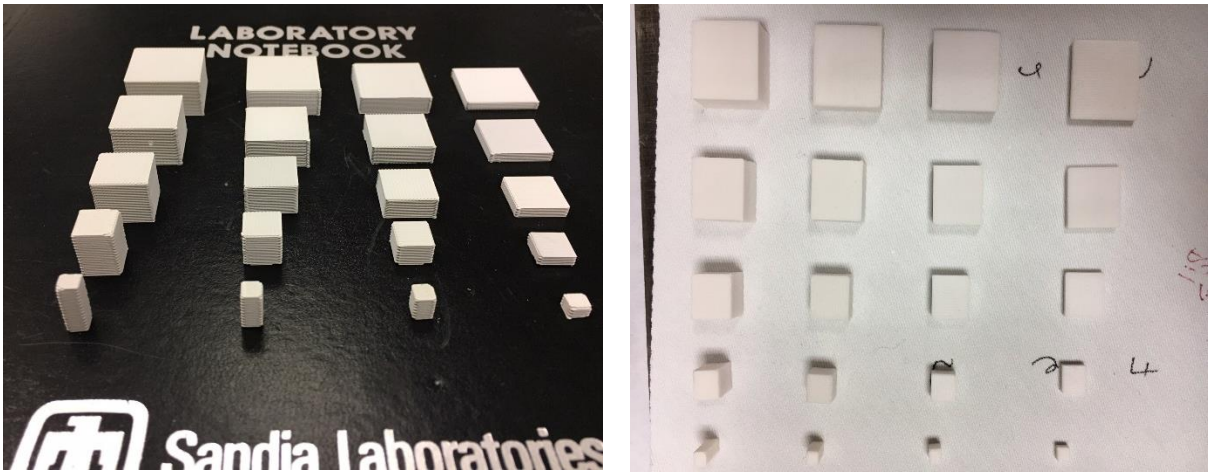

Figure 4.6. Alumina demonstrator cubes as printed (left) and after sintering (right).

Table 4.1 shows the analysis of the process data across the 20 cubes. In this table, we compute the average syringe force, platen temperature, and extrusion temperature per each z-layer. The table then shows the overall mean (averaged over all z-layers) as well as the minimum and maximum z-layer value and the standard deviation. This gives some indication of the stability of the process. Note that the syringe force is the most variable, with cubes that have large standard deviation of syringe force highlighted in yellow. The syringe force has the largest coefficient of variation (standard deviation/mean): in some of the cubes, this is around 20%. However, the temperatures are much more consistent, with coefficient of variation less than 1% for platen temperature and approximately 0.2% for the extrusion temperature.

		Syringe Force (lbs)				Platen Temp C				Extrusion Temp C			
Cube #	Num Layers	Mean	Max	Min	Std Dev	Mean	Max	Min	Std Dev	Mean	Max	Min	Std Dev
1	74	25.26	28.09	23.93	1.21	116.60	135.67	110.54	9.03	172.33	173.64	167.74	1.33
2	83	35.75	44.22	22.59	6.01	138.22	138.93	137.57	0.33	177.05	177.74	176.38	0.31
3	78	21.96	26.47	13.61	3.15	131.72	137.21	128.76	2.79	176.60	177.37	175.95	0.29
4	77	32.99	34.45	29.14	1.32	133.56	134.40	132.22	0.51	176.66	177.60	175.80	0.41
5	73	21.14	22.80	16.31	1.51	136.83	137.69	135.80	0.49	176.23	177.08	175.53	0.42
6	53	33.20	45.38	19.49	5.11	126.88	130.53	116.18	2.67	173.28	174.18	172.51	0.42
7	63	22.09	23.69	14.12	1.55	136.50	138.98	133.77	2.01	176.74	177.77	175.67	0.47
8	62	20.46	25.03	12.09	4.09	132.84	135.20	129.18	2.15	176.57	177.40	175.78	0.40
9	47	43.09	47.46	33.92	3.04	131.74	132.65	130.89	0.51	176.59	177.22	176.11	0.25
10	49	21.92	22.55	20.85	0.41	136.14	136.68	135.73	0.26	176.25	177.15	175.41	0.60
11	48	26.20	32.39	14.54	5.09	134.80	136.89	132.79	1.04	176.63	178.61	175.67	0.64
12	59	18.30	20.45	13.94	2.31	134.93	138.43	131.54	2.54	176.40	176.76	176.04	0.17
13	41	21.07	23.13	10.97	2.29	136.56	137.97	134.72	0.70	178.16	179.88	177.05	0.83
14	34	21.96	23.63	17.80	1.36	135.09	135.86	134.18	0.43	176.96	177.71	175.92	0.40
15	33	23.31	23.73	22.22	0.28	135.97	136.66	135.37	0.42	175.78	176.03	175.51	0.15
16	45	27.11	31.78	23.38	2.69	134.56	138.75	131.87	2.18	177.09	177.43	176.75	0.16
17	21	25.94	27.31	23.34	1.44	111.61	112.82	110.46	0.73	174.30	175.44	173.82	0.37
18	28	24.93	26.42	22.62	1.48	134.19	135.25	132.68	0.69	176.64	177.11	176.12	0.23
19	16	19.97	20.49	18.83	0.50	131.41	132.42	130.08	0.80	173.48	173.90	173.16	0.22
20	16	22.70	23.02	21.83	0.30	136.77	137.04	136.50	0.15	175.65	175.82	175.55	0.10
OVERALL AVERAGE		25.47	28.62	19.78	2.26	132.35	135.00	130.04	1.52	175.97	176.79	175.12	0.41

Table 4.1 Process Data for 20 Direct Write Alumina Demonstrator Cubes. Syringe force, platen temperature, and extrusion temperature are averaged per z-layer, and this table presents summary statistics across the z-layers. Note that some of the cubes have different numbers of layers due to their differing size (see Figure 4.6).

The CT images on the demonstrator cubes were processed and analyzed to obtain number of pores per layer for cube 4 (one of the large cubes). This data was then correlated with the pressure data. The results here differ from the insulator ring results. In the cubes, the pressure increases in z-direction as the cube is created. With all layers, the correlation of z-position with syringe force is 0.75 (strong positive correlation as seen in the right side of Figure 4.7). If we remove the bottom 16 layers for start-up effects, a positive correlation remains (0.53). However, the number of pores decreases slightly per layer. The correlation of z-position with respect to number of pores is -0.19. The side-by-side comparison is shown in Figure 4.7. To get a better sense of the trend of number of pores as a function of z-direction, we plot the data with a regression line in Figure 4.8. The linear fit has a very small negative slope, indicating the average number of pores per z-slice decreases slightly as the build proceeds. Note, however, there are large number of pores in the very top layers.

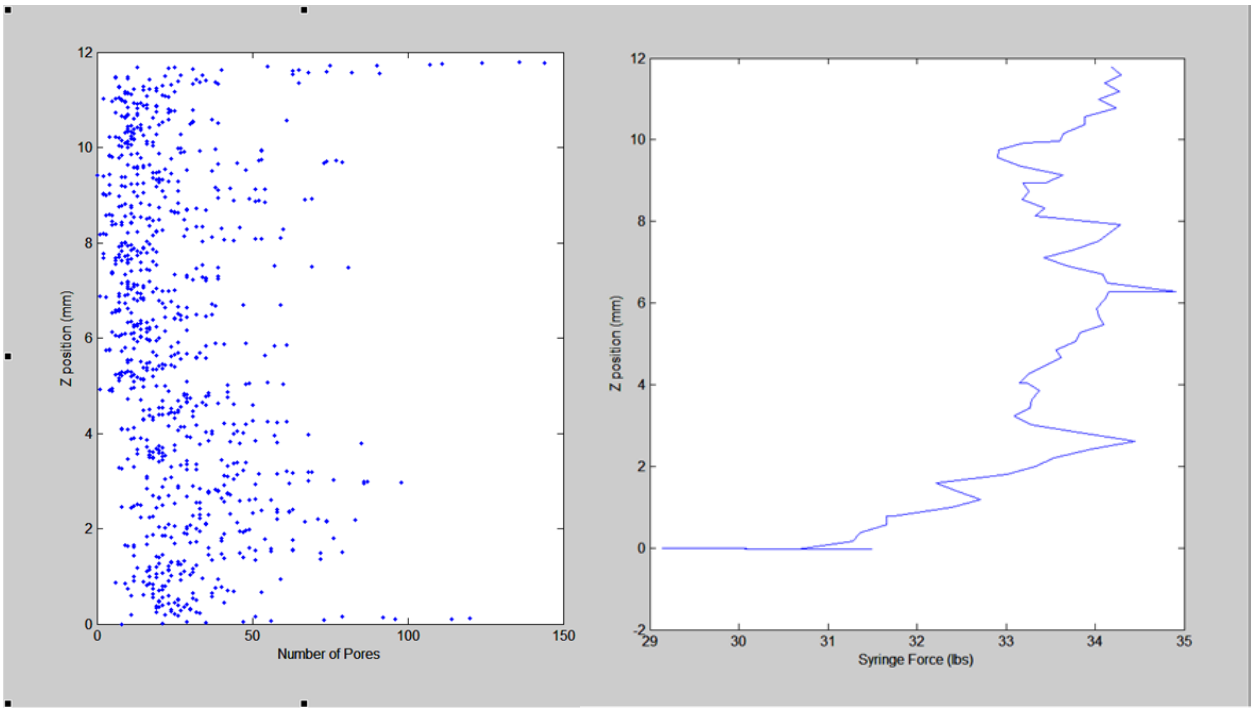

Figure 4.7. Number of pores as a function of Z-layer (left) and syringe force as a function of z-layer (right).

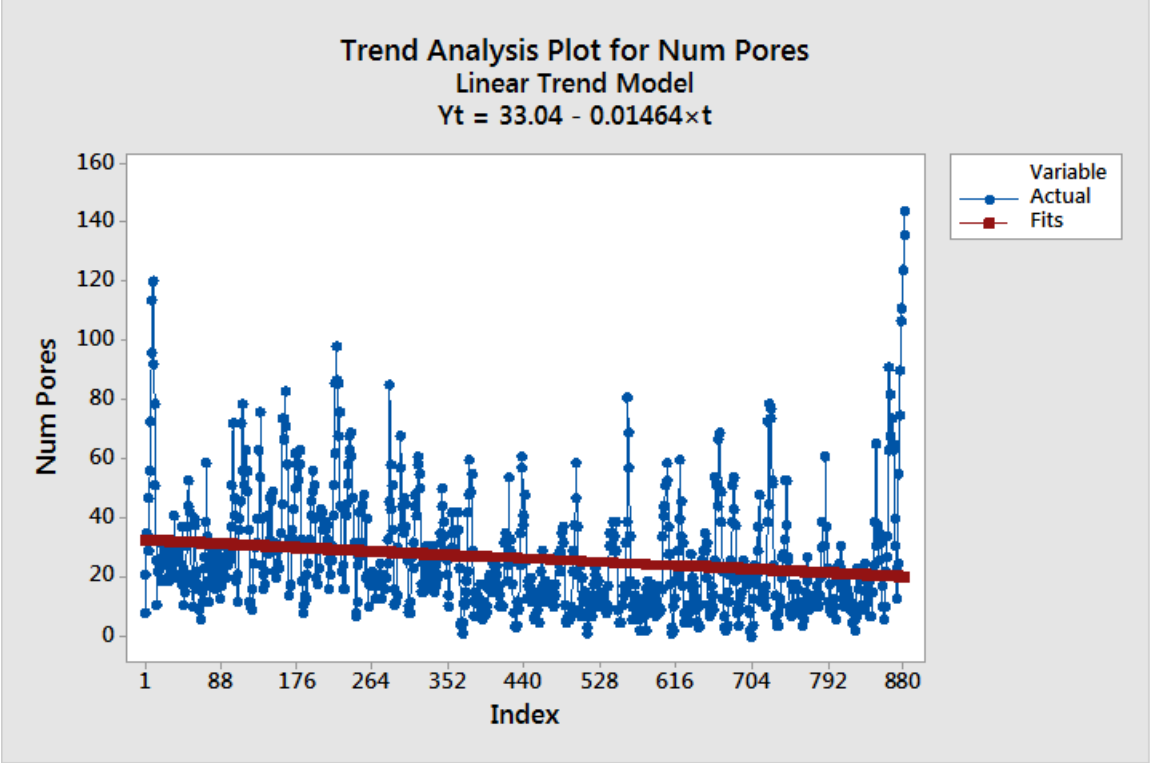

Figure 4.8. Trend analysis for number of pores vs. layer number from CT data.

4.3. Bend Bars

The Direct Write process was also used to print bend bars used for tensile testing. The bars were printed in three orientations as shown in Figure 4.9:

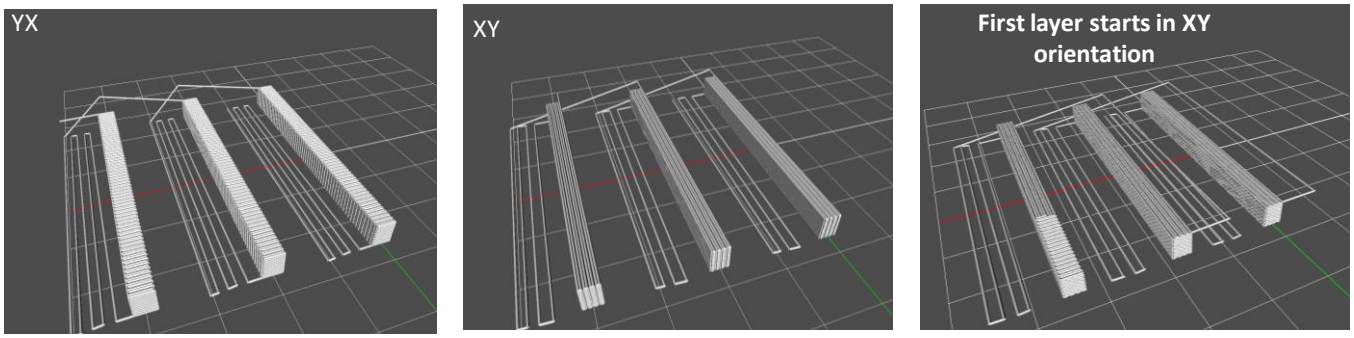

Figure 4.9. Three build orientations for Direct Write printing of tensile bars. The last orientation (on right) is a "cross-hatch" pattern, which varies XY and YX orientations in every other layer.

A Weibull analysis of yield strength for the three build orientations is shown in Figure 4.10. This figure shows that there are statistically significant differences in yield strength due to build orientation, with the YX orientation exhibiting the lowest yield strength and the XY orientation the highest yield strength. Furthermore, the characteristic strength values for the three orientations as shown on the plot are: 161 MPa (YX), 195 MPa (90) and 209 MPa (XY). In all cases, the probability of the yield strength being less than 70MPa is very small. The results of this testing provides important information for the continuum models. It also provides a lesson across additive manufacturing processes about the critical role of build orientation in mechanical properties. For example, if one compares Figure 4.10 to Figure 3.9 (a similar figure from LENS showing significant yield strength differences across build orientations), we see a similar graph. This highlights the need to carefully consider the role of build orientation.

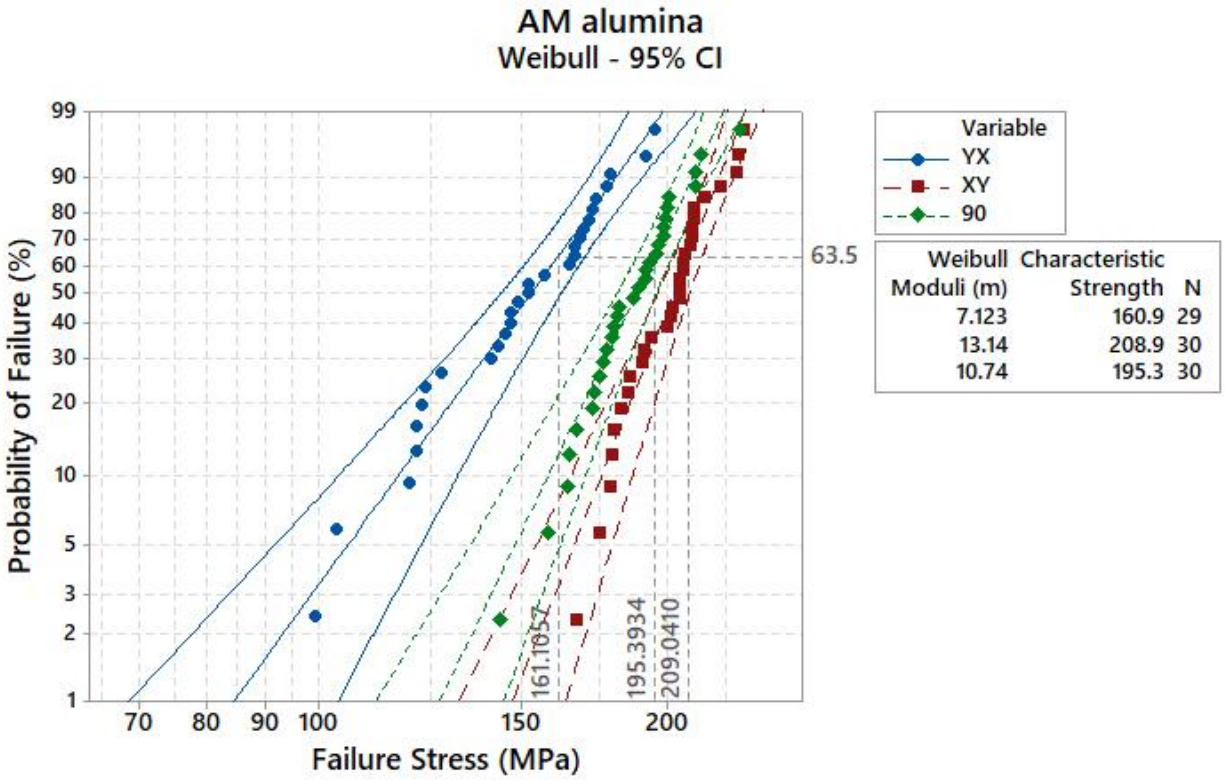

Figure 4.10 Weibull fits of three build orientations for Direct Write printing of Alumina tensile bars.

5. SUMMARY

This report summarizes the data analysis activities that were performed under the Born Qualified Grand Challenge Project from 2016-2018. The Born Qualified vision describing how data science and uncertainty quantification are central to materials characterization, part characterization, process characterization and in-situ monitoring, modeling at all scales, and design and optimization is outlined in Chapter 1. The particular additive manufacturing processes (powder bed, LENS, and direct write) were described in Chapters 2-4. Depending on the data available and the particular process and parts involved, each chapter described data analysis and characterization for parts, processes, and simulation models. Where possible, correlation analysis and more advanced statistical methods were used to relate process characteristics to part properties or to relate microstructure information to gross material properties.

There is much to be done to advance data analysis for AM parts and processes. The capability to manufacture parts quickly is a great advance of additive technologies. However, the data analysis for the high-resolution measurements such as micro computed tomography (micro CT) and melt pool imaging is time-consuming and challenging. For example, it is a labor intensive process to learn how to threshold and segment micro CT images, how to properly register and align stacks of images for comparison across parts, and how to extract quantities such as pores in a certain region with a certain size. Another example is given by the images of the melt pool produced (for example) from a two-color pyrometer during an AM build. One build of a small part such as a 10mm tensile bar may have 100K images of a melt pool. These are temporally generated images which have to be "stitched together" in some way if one is trying to compare the melt pool with micro CT data, which will be a static TIFF stack taken after the part is built. The volume of data now available from high-resolution measurements is huge. Micro-CT scans can now be performed at 3 micron voxel resolution, resulting in gigabytes of data if one saves all the images from a few parts. Note that before one can do any statistical analysis, uncertainty characterization, or data analytic machine learning, the data sets themselves have to be processed. Data processing often takes more time than data analysis.

We need better ways of performing in-situ data analysis, to identify and save salient features and reduce the data stream while it is being generated. We need better methods to automate the image analysis of AM parts. And finally, we need to draw on the rich set of algorithms that are being developed in the data science and data analytics community. These include ways of reducing a high resolution set of 3-D images to spatial statistics which describe various spatial correlation functions [12,13], and algorithms that can reduce the dimension of high-resolution temporal and spatial data easily to a small set of basis vectors or other features using principal component analysis or other dimension reduction methods. We also need to develop methods that can learn from temporal and spatial information about part temperature and porosity (for example) and relate that to material properties such as yield strength and residual stress.

Finally, we want to emphasize the need to save the massive amount of data being generated experimentally and with simulations of AM parts and processes. As part of

this LDRD project, we established a data repository which will be described in a companion memo. Most scientific work is still saved in a relatively flat file structure, with files stored in a hierarchical directory structure. Modern data storage is moving in a different direction, with cloud computing, heterogeneous and distributed storage, and storage of objects such as images or movies, not just files. Databases now store metadata which can be queried to point to the location of the actual object or files that need to be retrieved. There is a broad need for data management solutions, including advanced data storage, data archiving, development of policies on data management, using data storage methods that improve the searchability of data, and development of revision controls and access controls on data. Additionally, we need to consider co-locating data management/storage with computing environments so they can be accessed concurrently for certain activities such as calibration or validation of high-resolution simulations using high-resolution experimental data and/or advanced data analytic/machine learning methods. These data management, archiving, storage, and structuring issues are challenges faced broadly in the scientific community, but additive manufacturing provides a great use case because of the vast amount of data which can be generated quickly given the relatively fast build times.

REFERENCES

[1] Seifi M, Salem AA, Beuth J, Harrysson OL, Lewandowski JJ, "Overview of materials qualification needs for metal additive manufacturing," *JOM*, 68(3) 747-764, March 2016.

[2] Seifi, M. Gorelik, M., Waller, J., Hrabe, N, Shamsaei, N, Daniewicz, S., and Lewandowski, JJ. "Progress Towards Metal Additive Manufacturing Standardization to Support Qualification and Certification", *JOM* 69(3) 439-455.

[3] Paul R, Anand S and Gerner F, Effect of thermal deformation on part errors in metal powder based additive manufacturing processes, *ASME. J. Manuf. Sci. Eng*. 136 031009, 2014.

[4] Salzbrenner BC, Rodelas JM, Madison JD, Jared BH, Swiler LP, Shen YL, Boyce BL, "High-throughput stochastic tensile performance of additively manufactured stainless steel", *Journal of Materials Processing Technology*, 2017, 241, pp. 1-12.

[5] Agrawal A, Choudhary A, "Perspective: Materials informatics and big data: Realization of the "fourth paradigm" of science in materials science," *APL Materials*, 4, 053208, 2016.

[6] Prater T, "Database development for additive manufacturing," *Progress in Additive Manufacturing*:1-8, 2017.

[7] Hu Z, Mahadevan S, "Uncertainty quantification and management in additive manufacturing: Current status, needs, and opportunities," *International Journal of Advanced Manufacturing Technology*, 93: 2855, DOI 10.1007/s00170-017-0703-5, July 2017.

[8] Lopez F, Witherell P, and Lane B. "Identifying Uncertainty in Laser Powder Bed Fusion Models." *Journal of Mechanical Design*, Vol. 138(11), 2016.

[9] Gholaminezhad I, Assimi H, Jamali A, and Ashouri D. "Uncertainty quantification and robust modeling of selective laser melting process using stochastic multi-objective approach." *Int J Adv Manuf Technol* (2016) 86:1425–1441.

[10] Choi S-K, Gorguluarslan RM, Park S-I, Stone T, Moon JK, and Rosen DW. "Simulation-Based Uncertainty Quantification for Additively Manufactured Cellular Structures." *Journal of Electronic Materials*, Vol. 44, No. 10, 2015, pp. 4035-4041.

[11] Jared BH, Aguilo MA, Beghini LL, Boyce BL, Clark BW, Cook A, Kaehr BJ, Robbins J, Additive manufacturing: Toward holistic design, *Scripta Materialia* 135, 141–147, 2017.

[12] Torquato, S. *Random Heterogeneous Materials*. Springer 2002. ISBN 978-1-4757-6355-3.

[13] Kalindindi, S. *Hierarchical Materials Informatics: Novel Analytics for Materials Data*. Butterworth-Heinemann, 2015. ISBN 978-0124103948.

[14] Yu S, Zhang Y, Wang C, et al. "Characterization and Design of Functional Quasi-Random Nanostructured Materials Using Spectral Density Function." *ASME. J. Mech. Des.* 2017. Vol. 139(7):071401-071401-12. doi:10.1115/1.4036582.

[15] King WE, Anderson AT, Ferencz RM, Hodge NE, Kamath C, Khairallah SA, Rubenchik AM," Laser powder bed fusion additive manufacturing of metals; physics, computational, and materials challenges," *Applied Physics Reviews* 2 (4):041304, December 2015.

[16] B. L. Boyce, B. C. Salzbrenner, J. M. Rodelas, A. M. Roach, L. P. Swiler, J. D. Madison, B. H. Jared and Y.-L. Shen, "Extreme-Value Statistics Reveal Rare Failure-Critical Defects in Additive Manufacturing," *Advanced Engineering Materials* **19** (8), 1-10 (2017).

[17] Madison, J, Underwood O, Swiler L, Boyce B, Jared B, Rodelas J, Salzbrenner B, "Corroborating Tomographic Defect Metrics with Mechanical Response in an Additively Manufactured Precipitation-Hardened Stainless Steel", AIP Conference Proceedings *Review of Progress in Quantitative Nondestructive Evaluation*, Vol. 37, 2017.

[18] Jared, B.H., Boyce, B.L., Madison, J.D., Ostein, J.T., Rodelas, J.M., Salzbrenner, B., Swiler, L.P., Underwood, O., and S. Dejong. "Defect Characterization for Material Assurance in Metal Additive Manufacturing." SAND2017-13190. OUO.

DISTRIBUTION

1	MS0156	Olga B. Spahn	2241
1	MS0346	Joseph E. Bishop	1556
1	MS0828	Sophia Lefantzi	1516
1	MS0878	Carlton F. Brooks	2585
1	MS0887	Shawn M. Dirk	1830
1	MS0889	Cole Yarrington	1851
1	MS0959	Deidre Hirschfeld	1832
1	MS1323	Daniel Z. Turner	1441
1	MS1318	James R. Stewart	1440
1	MS1315	Ryan Wixom	1881
1	MS1349	P. Randall Schunk	1815
1	MS1411	Ryan P. Haggerty	1816
1	MS0899	Technical Library	9536 (electronic copy)
1	MS0359	D. Chavez, LDRD Office	1911


Sandia National Laboratories